Computers and Fluids 280 (2024) 106345

Contents lists available at ScienceDirect

Computers and Fluids

journal homepage: www.elsevier.com/locate/compfluid

On the generation of free-stream turbulence at low Reynolds number: A numerical study

J.M. Catalán [a], S. Olivieri [a,*], M. García-Villalba [b], O. Flores [a]

[a] Department of Aerospace Engineering, Universidad Carlos III de Madrid, Spain
[b] Institute of Fluid Mechanics and Heat Transfer, Technische Universität Wien, Austria

ARTICLE INFO

Keywords:
Turbulence
Direct numerical simulation
Synthetic
Digital filtering
Immersed boundary method
Low-Reynolds aerodynamics

ABSTRACT

We investigate the generation of free-stream perturbations at a relatively low characteristic Reynolds number of 1000 by means of direct numerical simulations using a synthetic turbulence generation method. This approach consists of generating turbulent fluctuations by means of digital filtering and a source term formulation in the Navier–Stokes equations. To assess its validity in the framework of decaying turbulence, we compare the results with those obtained with a physically-based, grid-induced turbulent flow in terms of spatial decay, evolution of characteristic length-scales and energy spectra. Also, we highlight relevant differences such as those in the streamwise development length and the anisotropy of the largest scales. Then, we characterize the generated perturbations when systematically varying the input parameters, namely the initial integral length-scale and turbulence intensity. Here, we notice differences in the streamwise decay of the turbulence intensity and the development length as we vary these parameters. By inspecting the evolution of the characteristic length-scales and the micro-scale Reynolds number, we also identify that the effective scale separation is highly sensitive to these variations.

1. Introduction

Atmospheric turbulence and, more in general, external flow perturbations are a well-known concern for many problems in aerodynamics and fluid–structure interaction. Indeed, with respect to the case of a uniform and unperturbed free stream, disturbances in the incoming flow can trigger particular phenomena or substantially alter the system dynamics. Examples include the effect that flow disturbances can exert on the shear layer transition and aerodynamic force generation for flows over bluff bodies [1–3] as well as wings or other streamlined shapes [4,5]. In this regard, some of these mechanisms have also been addressed from a more fundamental viewpoint, assessing the influence of free-stream turbulence on the development and transition of boundary layers [6–9].

As opposed to some classical applications, in which the typical size of the energy-containing turbulent eddies present in the flow is orders of magnitude below the characteristic length of the problem (high Reynolds number), a quite recent interest is devoted to problems involving flows at relatively low Reynolds number, where these two scales become comparable. This is motivated by the appearance of increasingly relevant applications such as micro-aerial vehicles (MAVs) or small-size drones [10,11], small-scale energy harvesting [12] and ocean engineering and marine science applications [13], thus representing a condition intrinsically different from those experienced by more conventional applications. Focusing on the aerial applications, such devices typically have centimetric sizes and are designed to operate at low speeds and low altitudes well within the atmospheric boundary layer (ABL). When comparing their low operational speed to the turbulent fluctuations typically present in the ABL, they can experience remarkably high turbulence intensity conditions that can have a dramatic influence on the aerodynamic performance [14,15]. As a result, a thorough understanding on how atmospheric turbulence affects the aerodynamic response of small-scale low-Reynolds devices has still not been achieved [16,17].

To tackle such an open topic, the essential prerequisite is the ability to generate free-stream turbulent perturbations with well-defined and controllable properties (e.g., turbulence intensity, statistical homogeneity and isotropy, scale-by-scale energy distribution). Indeed, the topic has a longstanding relevance in fluid mechanics, dating back to the early work by Batchelor and Townsend [18]. In the experimental practice, the generation of turbulence in a wind tunnel is typically achieved by means of passive or active systems. A classical example of the former is the use of solid grids at the inlet of the test chamber [19,20]. For the

* Corresponding author.
E-mail address: solivier@ing.uc3m.es (S. Olivieri).

https://doi.org/10.1016/j.compfluid.2024.106345
Received 15 March 2024; Received in revised form 30 April 2024; Accepted 15 June 2024
Available online 24 June 2024

latter, both active grids and jet arrays have been proposed, with the goal of effectively increasing the achieved turbulence level [21–23].

In the context of computational fluid dynamics (CFD), different techniques have been proposed in order to impose free-stream perturbations with desirable and physically sound properties, often fulfilling those of fully developed turbulence. From a historical perspective, two main approaches, namely recycling and synthetic, have been proposed and widely employed over the last decades, as extensively reviewed by Wu [24]. In a recycling approach, a turbulent flow is usually generated in an auxiliary simulation and later used as an input for the main simulation. A relevant example of recycling methods is the work of Lund et al. [25], which proposed to generate time-dependent turbulent inflow data for simulations of spatially developing boundary layers by using auxiliary simulations. In this work, the authors recycle the turbulent velocity field from a station near the domain exit of the auxiliary simulation and re-introduce it as the inflow boundary condition. This approach was later refined by Pierce [26], who introduced a corrective body-force technique that allows the turbulence statistics of a simulation of spatially periodic channel to be matched to arbitrarily prescribed statistics. Such a method was employed for example in computations of boundary layer flows over smooth obstacles [27].

In a synthetic approach, on the other hand, turbulence is generated artificially on the fly as the simulation is running, thus avoiding the need for an auxiliary simulation. In this field, a seminal contribution was provided by Juneja et al. [28], who originally showed how to artificially prescribe velocity fluctuations with statistical properties closely resembling those of real turbulence. Based on the same concept but with different features, several approaches to generate inflow perturbations have later been proposed, e.g., prescribing a given energy spectrum [29] or a superposition of coherent structures [30–32].

Among the synthetic approaches, Klein et al. [33] introduced a technique that relies on digital filtering for creating turbulent inflow conditions for spatially developing simulations. Several subsequent works adopted this method [34–37]. In a further development, Kempf et al. [38] modified Klein et al. [33]'s method to enhance its computational efficiency.

Incorporating concepts from both Klein et al. [33]'s method and Kempf et al. [38]'s modification, Schmidt and Breuer [39] introduced a variation of the technique in which flow perturbations are not imposed at the inlet boundary, but are instead generated through a source term integrated into the Navier–Stokes equations. The notable advantage of this approach is that it allows for the utilization of coarser grid resolutions in the upstream region, since the fluctuations are introduced directly in the vicinity of the area of interest, where the body to be tested is placed. This method avoids the dissipation of the fluctuations that can potentially take place if the distance between the inlet and the body is too large. Breuer [40] demonstrated the advantages of this approach, showcasing its suitability in studying the impact of free-stream turbulence on the flow characteristics over an airfoil featuring a laminar separation bubble.

As another possibility that differs from the approaches discussed so far, a few studies have explored the concept of fully-resolved simulations where the presence of a solid grid is explicitly reproduced, thus directly mimicking the setting that is typically used in wind tunnels for the generation of free-stream turbulence. The first attempt in this regard was presented by Djenidi [41] in a rather idealized configuration (i.e., considering an array of floating plates normal to the incoming flow). Later, a limited number of studies have considered more realistic geometries, including classical (e.g., monoplane square grids) as well as fractal grids [42–45]. Given the direct analogy with the experimental counterpart, it can be highlighted the physically-based nature of this approach.

In this work, we aim at characterizing the free-stream perturbations that can be generated using a synthetic turbulence (ST) approach. To this end, we employ direct numerical simulations (DNS) to quantify relevant flow features in terms of the decay of turbulence intensity, spectral energy distribution and spatial evolution of the characteristic length-scales of the flow. Firstly, we present a comparative assessment with respect to the flow generated by means of a physically-based, grid-induced turbulence (GT) approach. Then, we characterize the most relevant properties of the perturbations generated with the present ST approach by means of a parametric study over its input parameters.

The rest of the paper is structured as follows: Section 2 describes the employed methodology, Section 3 contains the main results of the study, and finally Section 4 draws some conclusions.

2. Methodology

We consider a Newtonian fluid governed by the Navier–Stokes equations for an incompressible flow,

$$\nabla \cdot \mathbf{u} = 0, \tag{1}$$

$$\frac{\partial \mathbf{u}}{\partial t} + (\mathbf{u} \cdot \nabla)\mathbf{u} = -\frac{1}{\rho}\nabla p + \nu \nabla^2 \mathbf{u} + \mathbf{f}_{\mathrm{st}} + \mathbf{f}_{\mathrm{ibm}}. \tag{2}$$

Here, $\mathbf{u} = (u, v, w) = (u_1, u_2, u_3)$ is the velocity, p the pressure, ρ the density and ν the kinematic viscosity. Two external forcing terms are included in the above equations, $\mathbf{f}_{\mathrm{st}}$ is the forcing term to introduce synthetic turbulence (Section 2.1) and $\mathbf{f}_{\mathrm{ibm}}$ is the forcing term that models the presence of the passive grid, using an immersed boundary method (Section 2.2). We define a Reynolds number based on the free-stream velocity U_∞ and a reference length-scale L, $\mathrm{Re} = U_\infty L/\nu$.

2.1. Synthetic turbulence

The approach under consideration in this work is a *synthetic turbulence inflow generator* (STIG). Specifically, we consider the implementation based on digital filters where the flow is forced by means of a source term $\mathbf{f}_{\mathrm{st}}$ active in a relatively narrow region of influence [33,38,39]. Here, the region of influence is located shortly after the inlet of the computational domain and centered around $x = x_{\mathrm{st}}$, so that the generated fluctuations are advected downstream by the mean flow and fill almost completely the domain (Fig. 1 top). The source term takes the following form:

$$\mathbf{f}_{\mathrm{st}}(x, y, z, t) = \begin{cases} \frac{\mathbf{u}'(t,y,z)}{T_0} \exp\left(-\frac{\pi}{2}\frac{(x - x_{\mathrm{st}})^2}{\Lambda_0^2}\right), & \text{if} \quad -2\Lambda_0 \le (x - x_{\mathrm{st}}) \le 2\Lambda_0, \\ 0, & \text{otherwise}, \end{cases} \tag{3}$$

where $\mathbf{u}'$ is a fluctuation velocity and Λ_0 and T_0 are the integral length and time scale of the flow fluctuations, respectively. Additionally, the extent of the influence region in the streamwise direction is delimited by $x \in [x_{\mathrm{st}} - 2\Lambda_0, x_{\mathrm{st}} + 2\Lambda_0]$ to smoothen the transition with the laminar flow, whereas its extent in the lateral directions spans the full domain (see Fig. 1 top). In order to generate the perturbation velocity $\mathbf{u}' = (u', v', w')$, the digital filtering approach of Kempf et al. [38] is used. Further details on the generation of the perturbation velocity field $\mathbf{u}'$ can be found in Appendix A. See also [46] for an application of the methodology to the flow over a settling sphere. Taylor's hypothesis [47] relates the integral time scale T_0 with the integral length-scale Λ_0 and the incoming flow velocity U_∞, such that $T_0 = \Lambda_0/U_\infty$.

Remarkably, the fluctuations generated by the STIG are characterized by their (input) turbulence intensity TI_0 and the (input) integral length-scale Λ_0, two parameters that are explicitly set in the algorithm and can be easily varied, thus representing a convenient feature of this approach.

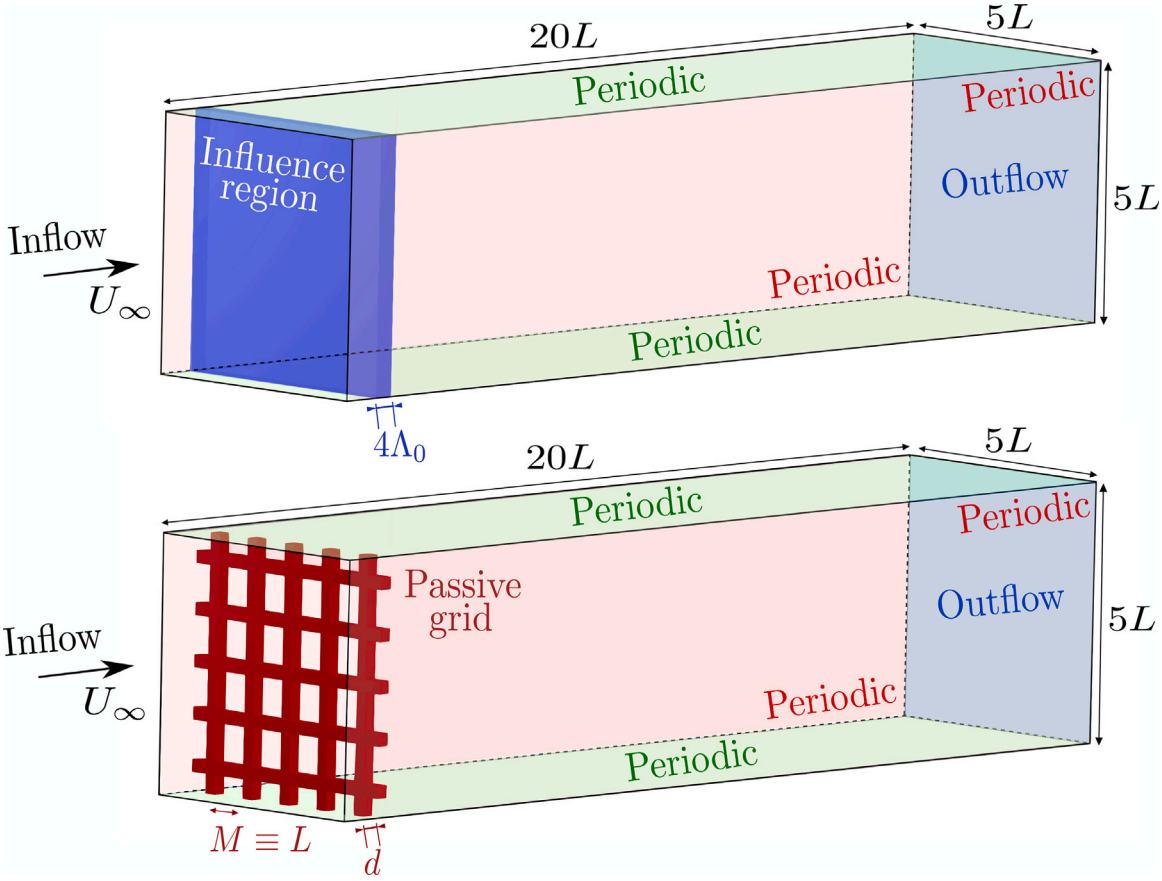

Fig. 1. Three-dimensional sketches of the computational domain and the boundary conditions, for the two different approaches presented: synthetic turbulence (top), grid-induced turbulence (bottom).

2.2. Grid-induced turbulence

To compare the results of the ST approach with an experimental-like flow configuration, we also consider the simulation of *grid-induced turbulence*. In this case, we model the presence of a solid passive grid located shortly after the inlet of the domain, essentially mimicking the typical setup adopted in wind tunnels (Fig. 1 bottom). Here, the geometry of the grid has a crucial influence on the properties of the generated turbulence in a way that is not explicitly known a priori [48], therefore representing a relevant difference with respect to the ST approach. On the other hand, such configuration ensures a physically based generation of the free-stream perturbations that can prove as a meaningful benchmark when directly compared to the ST results.

In order to achieve satisfactory flow properties (i.e., turbulence intensity, homogeneity and isotropy), we choose the SSQ43 geometrical configuration of Djenidi et al. [49]. It corresponds to a mono-plane grid made of rods with square cross-section of side d, which are evenly spaced by a distance $M = 4d$ (see Fig. 1 bottom). As a result, the grid solidity $\sigma = d/M\,(2 - d/M) \approx 44\%$. Note that we fix $M \equiv L$, i.e., the spacing between the rods is assumed as the reference length of the problem.

From the computational viewpoint the presence of the grid, and in particular the no-slip boundary condition between the fluid and the solid, is enforced by using the direct-forcing immersed boundary method (IBM) proposed by Uhlmann [50]. A nonconformal unstructured Lagrangian mesh is introduced for describing the geometry of the solid surface, at which the no-slip condition is indirectly applied by means of a forcing term (computed at the Lagrangian points). This forcing is then spread to the surrounding Eulerian grid points using the regularized delta function proposed by Roma et al. [51], eventually yielding the source term $\mathbf{f}_{\text{ibm}}$ appearing in Eq. (2).

2.3. Computational setup

The problem is tackled numerically using *TUCAN*, an extensively validated, massively parallel in-house code [52–54]. The code solves the Navier–Stokes equations of the incompressible flow, Eqs. (1) and (2) using a fractional-step method on a staggered Cartesian mesh. The spatial derivatives are discretized with centered, second-order accurate finite differences, whereas the time integration is performed by means of a semi-implicit low-storage three-stage Runge–Kutta method.

We choose a domain box ranging from $x/L = -1$ to 19 in the streamwise direction and from $y/L = z/L = -2.5$ to 2.5 in the transverse (homogeneous) directions, therefore having a size $20L \times 5L \times 5L$ (see Fig. 1). A uniform inflow U_∞ is imposed at the inlet ($x/L = -1$) whereas an advective boundary condition is imposed at the outlet ($x/L = 19$). Periodic boundary conditions are applied at the lateral boundaries normal to the transverse directions. For the comparison between the two approaches, both the influence region of the ST cases and the passive grid in the GT case are centered at $x/L = 0$ (i.e., for the ST cases we set $x_{\text{st}=0}$).

With the interest in relatively low-Reynolds-number flows, throughout this work we consider Re = 1000. We discretize the domain with a uniform spatial resolution Δ in all three directions. We assess the convergence of the results while doubling the resolution, as detailed in Appendix B. Consequently, for the comparative study presented in Section 3.1 we use the higher resolution $\Delta \approx 0.02L$ (according to the requirement posed by the GT case). For the parametric characterization

with the ST approach presented in Section 3.2, on the other hand, we can safely use the lower resolution $\Delta \approx 0.04L$ (as shown in Appendix B). Finally, the simulation time step is selected such that the maximum CFL number is always approximately 0.3.

2.4. Notation

To provide a statistical characterization of the flow we are going to use several quantities that are defined in this section. Firstly, we denote the fluctuating part of the velocity as $u_i'(\mathbf{x},t) = u_i(\mathbf{x},t) - \langle u_i \rangle$ (for the generic ith component), where $\langle\cdot\rangle$ indicates both temporal average and spatial average over the (y,z) cross-plane. Hence, we compute the root-mean-square of the velocity fluctuations for the streamwise, vertical and spanwise component as $u_{\text{rms}} = \langle u_1'^2 \rangle^{1/2}$, $v_{\text{rms}} = \langle u_2'^2 \rangle^{1/2}$ and $w_{\text{rms}} = \langle u_3'^2 \rangle^{1/2}$, respectively. Then, we define the turbulent kinetic energy as $TKE \equiv 1/2\,(u_{\text{rms}}^2 + v_{\text{rms}}^2 + w_{\text{rms}}^2)$ and the turbulence intensity as $TI \equiv \sqrt{2/3\,TKE}/U_\infty$. Another quantity of interest, often used to measure the (large-scale) anisotropy of the flow [20], is the ratio between the transverse and longitudinal velocity fluctuations $R \equiv (v_{\text{rms}} + w_{\text{rms}})/(2u_{\text{rms}})$, where the two transverse (i.e., vertical and spanwise) components, v_{rms} and w_{rms}, are here averaged since the configuration is invariant under a 90° rotation.

The integral length-scale Λ and the Taylor micro-scale λ are both obtained from the velocity autocorrelation functions using the standard definitions (see for example [55]). We either use the longitudinal autocorrelation function, $f(r) \equiv \langle u_i'(\mathbf{x})\, u_i'(\mathbf{x}+r\mathbf{e}_i)\rangle / \langle u_i'^2 \rangle$, or the transverse one, $g(r) \equiv \langle u_i'(\mathbf{x})\, u_i'(\mathbf{x}+r\mathbf{e}_j)\rangle / \langle u_i'^2 \rangle$, where we consider only the transverse velocity components, i.e., $i = \{2,3\}$ and $j = \{2,3\}$ with $j \neq i$, and the spatial separation r lies in the cross plane (y,z). Thus, in our notation, Λ_f and λ_f represent the longitudinal integral and Taylor length-scales while Λ_g and λ_g represent the transverse ones, respectively. The Taylor micro-scale Reynolds number is defined as $\text{Re}_\lambda \equiv u_{\text{rms}}\lambda_f/\nu$. The Kolmogorov length-scale is defined as $\eta \equiv (\nu^3/\epsilon)^{1/4}$. Here, the turbulent energy dissipation rate is defined as $\epsilon = 2\nu\langle S_{ij}S_{ij}\rangle$, where $S_{ij} = 1/2\left(\partial u_i/\partial x_j + \partial u_j/\partial x_i\right)$ (for $(i,j) = \{1,2,3\}$) is the strain rate tensor.

Finally, we look at the spectral properties of the generated fluctuations. For each velocity component u_i', we apply a two-dimensional Fourier transform along the periodic directions y and z, from which we obtain the (component-wise) energy spectrum $E_{ii}(x,\kappa_y,\kappa_z)$, where κ_y and κ_z denote the wavenumber vector components. We assume isotropy in the cross plane and average over circles of radius equal to $\kappa = \sqrt{\kappa_y^2 + \kappa_z^2}$, yielding $E_{ii}(x,\kappa)$ where the directional information on the wavenumber is removed [55]. Lastly, we introduce the total energy spectrum $E(x,\kappa) = \sum_{i=1}^{3} E_{ii}(x,\kappa)$.

3. Results

Using the described methodology, we have performed a series of six cases (five cases using the ST approach varying its input parameters, and one case using the GT approach), as summarized in Table 1. After preliminary testing , we have been able to select a combination of ST input parameters ($\Lambda_0/L = 0.15$, $TI_0 = 35\%$) such that the resulting flow has similar characteristics to the one generated in the GT00 case. Therefore, in the following, the case with those input parameters, ST1535, is denoted the baseline case. The analysis of the results is split into two parts. First, in Section 3.1, we perform a direct comparison between the GT and ST approaches. This is done by analyzing the results of the (high-resolution) baseline case, ST1535-A, and the solid grid case, GT00. Then, in Section 3.2, we focus on the ST approach to investigate the effect of the input parameters (Λ_0 and TI_0) on the main flow properties.

All the performed simulations have been integrated for at least 100 convective time units (i.e., L/U_∞), corresponding to more than 5 flow-through times. The computation of statistics is started after discarding an initial transient of at least $20L/U_\infty$. Quantities are spatially averaged in the homogeneous directions y and z. Additionally, temporal averages were computed using a minimum of 50 and 80 snapshots for the higher and lower resolution, respectively, with a $1.25L/U_\infty$ time separation between consecutive snapshots to ensure decorrelation.

Table 1
Designation of the cases considered in the simulation campaign. For the ST cases, the input parameters (i.e., Λ_0 and TI_0) are indicated. For all considered cases, the results of the fit with respect to the power-law Eq. (4) (i.e., x_0, x_i, n and A) are reported.

Case	Δ/L	Λ_0/L	TI_0	x_0/L	x_i/L	n	A
ST1535-A	0.02	0.15	35%	0.65	4.75	−1.34	0.105
ST1535-B	0.04	0.15	35%	0.1	3.25	−1.41	0.134
ST1035	0.04	0.10	35%	−0.1	2.00	−1.37	0.070
ST2035	0.04	0.20	35%	0.3	4.25	−1.42	0.210
ST1520	0.04	0.15	20%	−0.6	4.75	−1.47	0.105
ST1550	0.04	0.15	50%	0.2	2.50	−1.35	0.162
GT00	0.02	–	–	4.0	7.75	−1.33	0.086

3.1. Comparative analysis between ST and GT approach

Fig. 2 shows a visualization of the instantaneous flow obtained in the ST1535-A case (top panel) along with that of the GT00 case (bottom panel). Specifically, the flow's vortical structures have been represented by means of isosurfaces of the Q criterion (i.e., second invariant of the velocity gradient tensor [56]) at two different levels. At a first glance, the two flows appear qualitatively similar, especially when focusing on the region sufficiently downstream where the turbulence is properly developed. In particular, it can be noticed the similar trend in decreasing the intensity of the turbulent eddies (along with a less apparent increase of their characteristic size) while moving downstream. This is consistent with the well-known phenomenology of decaying turbulence.

However, some key differences can be noticed. The first concerns the degree of homogeneity of the flow on the development region, i.e., sufficiently close to the region of influence for the ST1535-A case or in the vicinity of the solid grid for the GT00 case. While the development region of the ST1535-A case is quite homogeneous, the GT00 case shows a coherent wake pattern downstream of the grid, resulting in a non-homogeneous flow. To better characterize this feature, we analyze in Fig. 3 the cross-planes of the time-averaged streamwise velocity component, $\bar{u}_x$, at various streamwise locations. As expected, for the ST1535-A case (top row of Fig. 3) the flow appears statistically homogeneous at all the considered locations, because the ST approach assures the homogeneity by construction. Conversely, for the GT00 case (bottom row) the signature of the wakes formed behind the rods composing the grid can be clearly recovered at $x/L = 1$. Nevertheless, such inhomogeneity progressively decreases while moving downstream, becoming approximately negligible for $x/L \gtrsim 5$.

A second remarkable difference between the ST and GT instantaneous fields in Fig. 2 regards the spatial development of the flow. Eddies of comparable intensity (having the same level of QL^2/U_∞^2 in Fig. 2) appear closer to the inlet plane for the ST case than for the GT case, so that the former appears to decay earlier. As it will be shown in the following, such difference in the characteristic development length is a relevant feature that needs to be properly accounted for when comparing the results of the two approaches.

The modeling of decaying turbulence relies on a well-known power-law expression for the TKE of the form

$$\frac{TKE}{U_\infty^2} = A\left(\frac{x - x_0}{L}\right)^n, \tag{4}$$

where A is a multiplicative factor, n is a (negative) decay exponent, and x_0 is a virtual origin [20,57]. Also, Eq. (4) can be recast for the TI as

$$TI = \sqrt{2/3\,A}\left(\frac{x - x_0}{L}\right)^{n/2}. \tag{5}$$

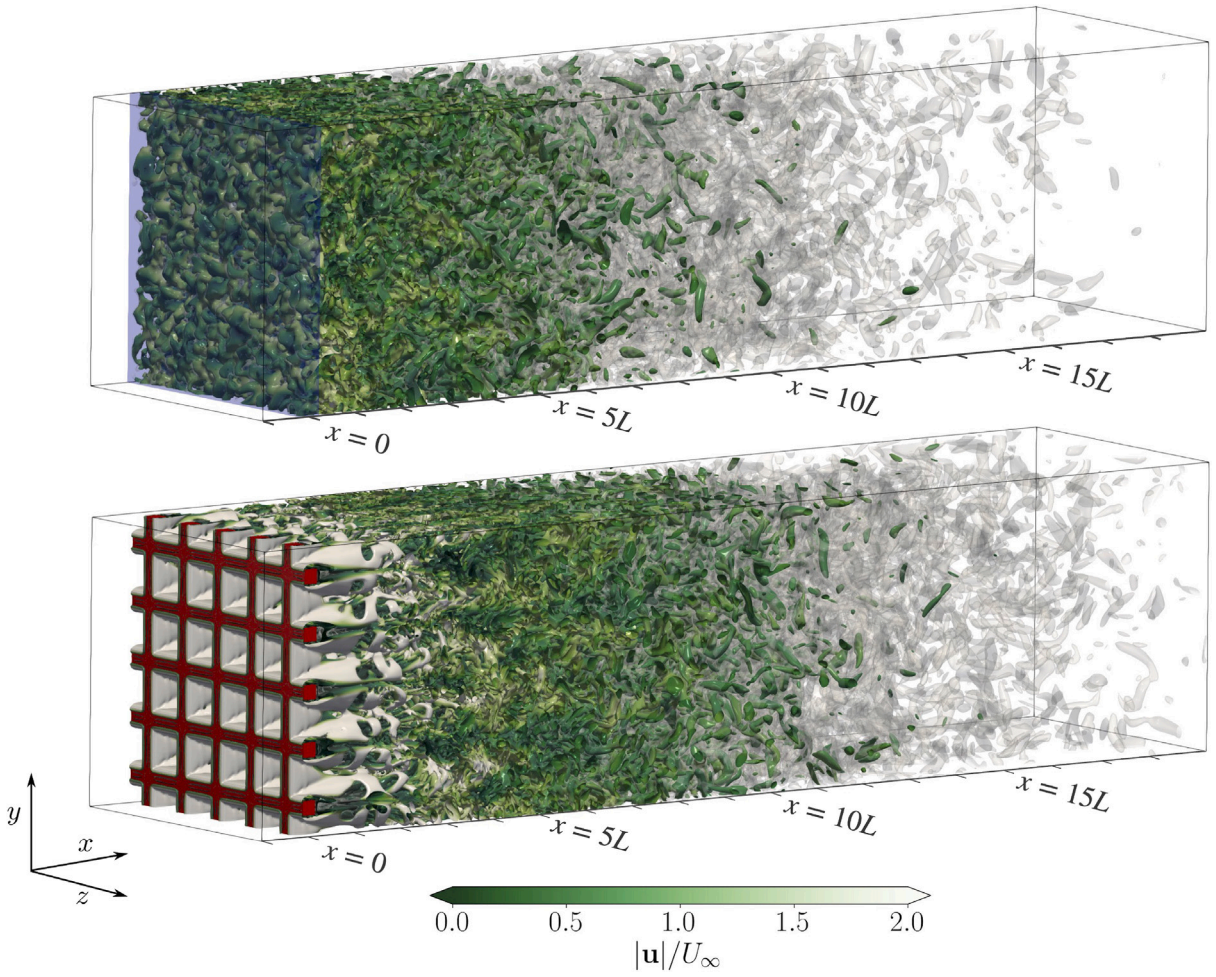

Fig. 2. Snapshots of the resulting turbulent fluctuations in the ST1535-A case (top) and GT00 case (bottom), flowing from left to right along the streamwise direction x. Both visualizations depict the instantaneous vortical structures by means of isosurfaces at $QL^2/U_\infty^2 = [1, 0.2]$. The higher value is colored using the magnitude of the velocity, while the lower one is colored in white and with a lower opacity. For the ST1535-A case, the transparent blue box indicates the region of influence where the source term $\mathbf{f}_{\text{st}}$ is active. For the GT00 case, the solid grid (whose presence is modeled by means of the source term $\mathbf{f}_{\text{ibm}}$) is colored in red.

We fit the numerical results to the power law, Eq. (4), employing the procedure proposed by Lavoie et al. [48] to reduce the uncertainty of the fit, as detailed in Appendix C. The results of the fitting procedure in terms of A, n and x_0, together with the approximate coordinate where the power-law decay begins, x_i, are collected in Table 1. Specifically, both the decay exponent and the virtual origin deserve some comments. Looking at the obtained values of $n \approx -1.33$, it can be observed that they satisfactorily agree with those reported in the literature at similar Reynolds numbers [49]. For the virtual origin x_0, on the other hand, the results are fully consistent with the qualitative scenario previously depicted (Fig. 2), showing a shorter development length for the ST1535-A case ($x_0 \approx 0.65L$, $x_i \approx 4.75L$) compared to the GT00 case ($x_0 \approx 4L$, $x_i \approx 7.7L$).

Fig. 4a shows the decay with streamwise direction of the TI when accounting for the virtual origin, showing a close agreement between the GT and ST approaches. This is clearly not the case when the virtual origin is not taken into account, see inset of Fig. 4a. As a consequence, the virtual origin is taken into account in all figures below, which show quantities as a function of the streamwise direction. Fig. 4a also includes lines corresponding to the power-law fits for both GT and ST, showing that the fit does an excellent job at approximating the numerical data for $(x - x_0)/L \gtrsim 4$, consistent with the extension of the development region estimated during the fit process, x_i, shown in Table 1.

The anisotropy of the flow, R, is shown in Fig. 4b. Here, a substantial difference between the ST1535-A and GT00 cases can be observed. The ST1535-A case shows an isotropic configuration (i.e., with R approaching 1) over the full extension of the domain. In contrast, for the GT00 case the anisotropy of the flow is remarkably higher, with a maximum value of $R \approx 0.9$ at $(x - x_0) \approx 5L$ and a profile of R along the streamwise direction that is less constant if compared to that of the ST1535-A case. In fact, this is a known feature of grid-induced turbulence [20,48]. Note that such anisotropy is typically observed to decrease as the nominal Reynolds number is increased [58,59]. Here, we consider a relatively low Reynolds number of 1000, for which anisotropy might be expected. In this respect, note also that suitable counteracting strategies (e.g., adopting a wind-tunnel contraction) have been proposed to reduce the flow anisotropy [19,20,48].

We turn now our attention to the relevant length-scales of the flow (i.e., integral, Taylor and Kolmogorov length-scale) along with the effective turbulent (i.e., micro-scale) Reynolds number, which are shown in Fig. 5 as a function of the streamwise coordinate. In particular, Figs. 5a and 5b present the integral length-scale Λ and the Taylor length-scale λ, respectively. Note that in each of these panels

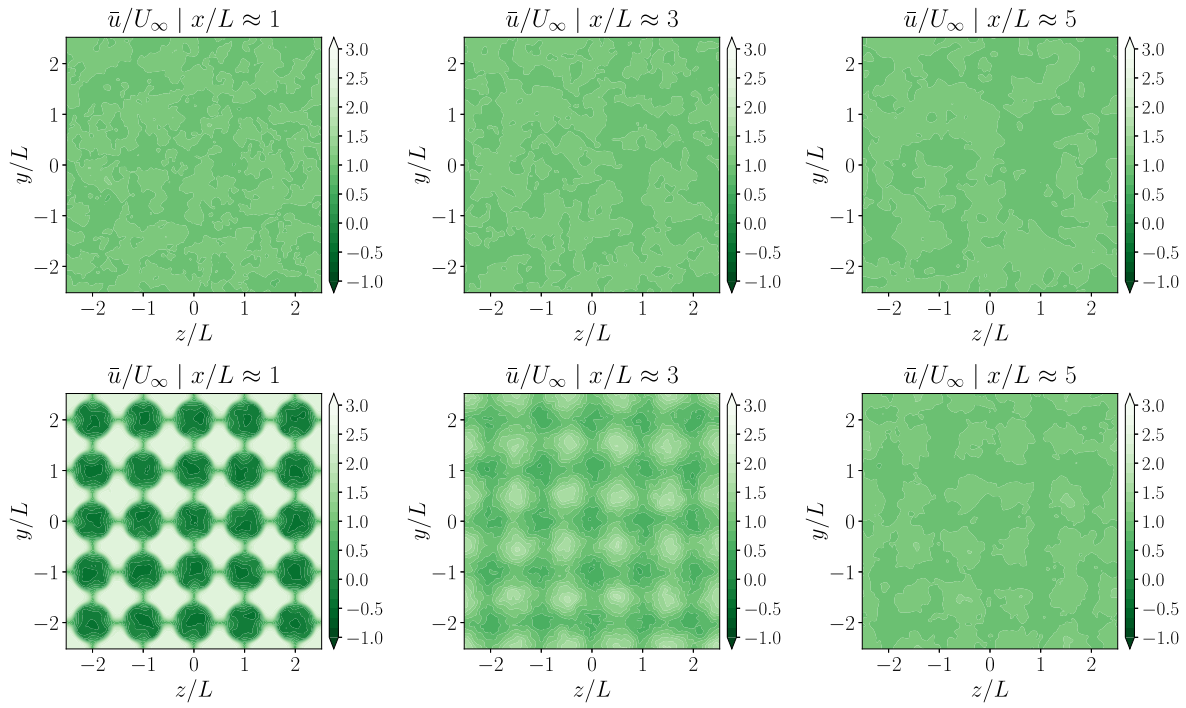

Fig. 3. Time average of the streamwise velocity component over cross planes at different streamwise locations $x/L = \{1, 3, 5\}$ (from left to right column) obtained in the ST1535-A case (top row) and GT00 case (bottom row).

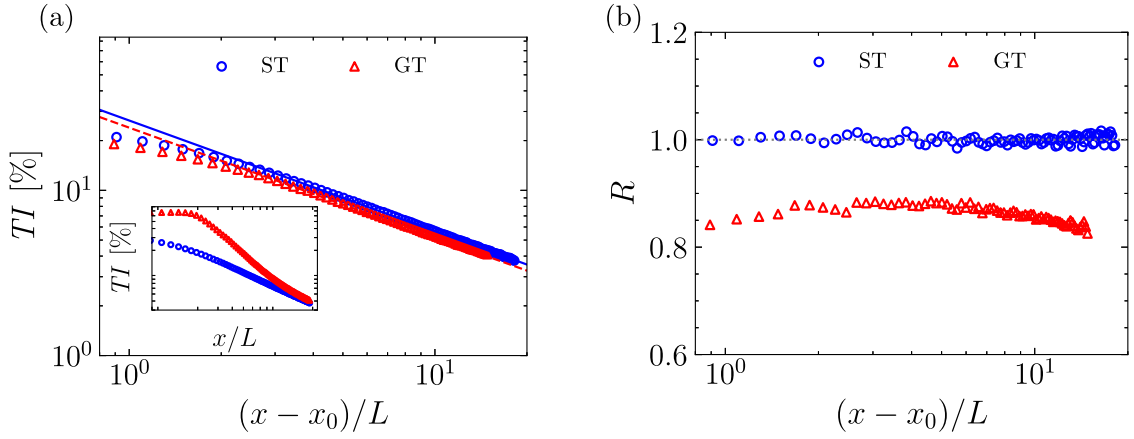

Fig. 4. Large-scale properties of the turbulent flow generated in the ST1535-A case (blue circles) and GT00 case (red triangles): (a) turbulence intensity; (b) large-scale anisotropy. In the main panels, quantities are plotted as a function of the streamwise coordinate corrected using the virtual origin x_0 (introduced in the text), whilst in the inset of (a) the turbulence intensity is shown as a function of the uncorrected coordinate. In (a), we also report the corresponding power-law decay, given by fitting the data against Eq. (5), both for the ST (blue solid line) and GT (red dashed line) approach.

we report both the longitudinal and transverse length-scale (as defined in Section 2.4). For isotropic turbulence, it holds that $\Lambda_f = 2\Lambda_g$ and $\lambda_f = \sqrt{2}\lambda_g$ [55]. We can test these predictions against our numerical results. For the integral length-scale (Fig. 5a) the agreement appears moderate for both ST1535-A and GT00, with $\Lambda_f > 2\Lambda_g$ for ST1535-A and $\Lambda_f < 2\Lambda_g$ for GT00. The disagreement is probably caused in both cases by the in-homogeneity of the flow in the streamwise direction, exacerbated in case GT00 by the lack of isotropy discussed in Fig. 4b. On the other hand, the agreement is very good for the Taylor length-scale (Fig. 5b), especially for sufficiently large $(x - x_0)$ where the flow has properly developed.

Next, we look at the characteristic length-scale at which the viscous diffusion is expected to be dominant, i.e., the Kolmogorov length-scale η. The spatial evolution of η is shown in Fig. 5c where the good agreement between the ST1535-A and GT00 case is confirmed, as it could also be expected when focusing on the smallest scales where the universal character of turbulence is well known. Lastly, Fig. 5d shows the streamwise evolution of the turbulent (or micro-scale) Reynolds number Re_λ, which serves to effectively measure the extent of scale separation in the generated turbulent flows. Consistently with the relatively low-Reynolds framework of our interest, the observed range of Re_λ is indeed $\mathcal{O}(10)$, indicating a rather limited scale separation.

Focusing now on the scale-by-scale energy distribution, Fig. 6 shows both the component-wise and total energy spectra computed at several locations within the region where the turbulent flow is properly developed. For the streamwise component spectra E_{uu} (Fig. 6a), a good agreement between the ST and GT case is found for all wavenumbers and every considered location. In contrast, for the transverse component spectra $E_{vv} \approx E_{ww}$ (Fig. 6b) the two cases are in reasonably good agreement only at sufficiently high wavenumbers (i.e., small scales) and some discrepancies can be observed for the lowest wavenumbers (i.e., at the largest scales). In particular, a higher energy content is

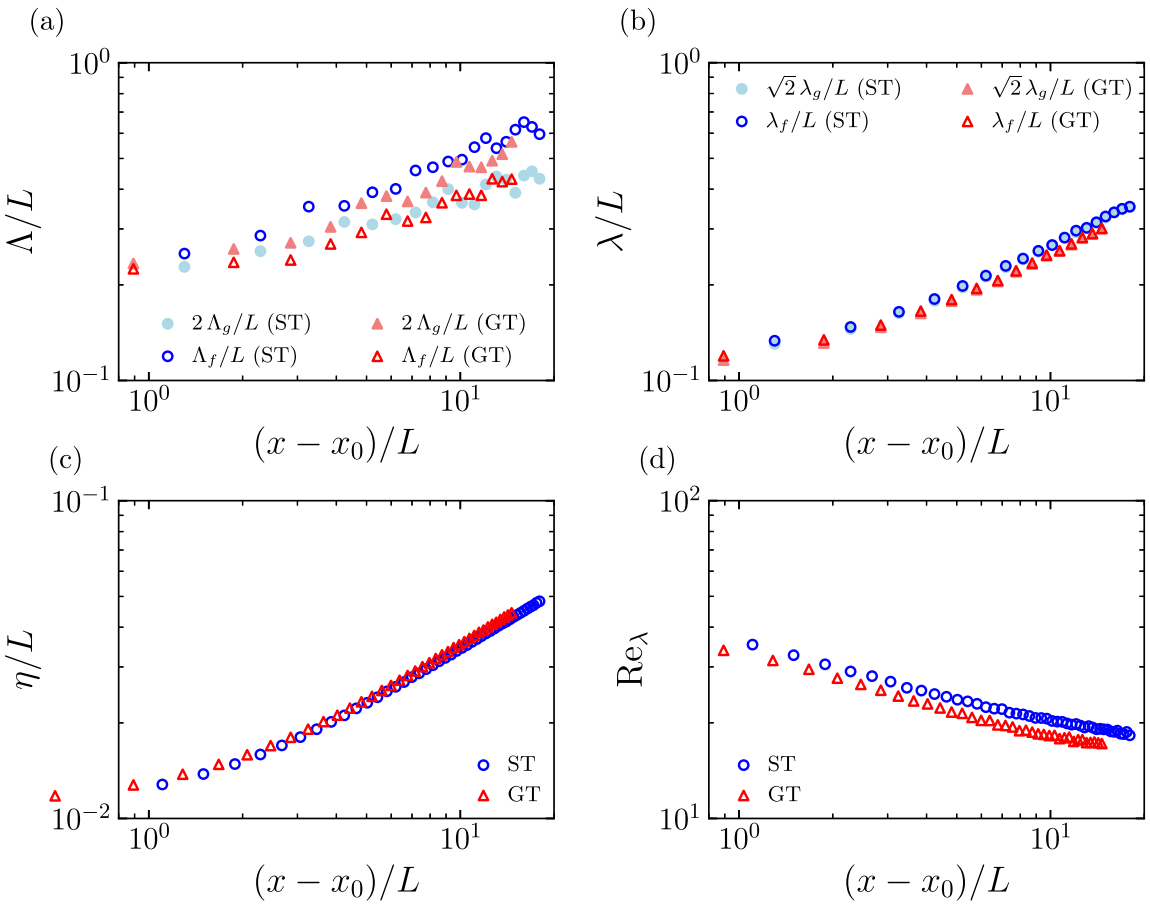

Fig. 5. Comparison of the characteristic length-scales and micro-scale Reynolds number between the ST1535-A case (blue circles) and GT00 case (red triangles), as a function of the streamwise coordinate $(x - x_0)$: (a) integral length-scales Λ and (b) Taylor length-scales λ (filled and empty symbols denote the longitudinal and transverse length-scale, respectively); (c) Kolmogorov length-scale η; (d) micro-scale Reynolds number Re_λ.

found for the ST results with respect to the GT ones. These differences are indeed consistent with the different degree of anisotropy discussed in Fig. 4b. Furthermore, Fig. 6c shows the total energy spectra normalized with the TKE (evaluated at the corresponding streamwise location) to better highlight the qualitative evolution of the energy distribution along the streamwise direction. The figure also includes the well-known $\kappa^{-5/3}$ scaling (gray dotted line) that is expected over the inertial subrange, showing a limited agreement with the present data. This is expected, given the low values of Re_λ of ST1535-A and GT00 (see Fig. 5d). On the other hand, the increasingly faster exponential decay at high wavenumbers when increasing $(x-x_0)$ reflects the decrease of Re_λ previously shown (Fig. 5d). Furthermore, in the insets of Fig. 6c we can also look at the premultiplied energy spectrum to highlight the most energetic wavenumbers. Specifically, it clearly appears that the dominant wavenumbers decrease while moving downstream, consistently with the increase in the integral length-scale of both cases (as shown in Fig. 5a).

Lastly, in Fig. 7 we compare the differences between the spectra of the ST1535-A and GT00 cases in the development region, where the fluctuations introduced in the flow adjust to the power-law decay. For the ST1535-A case, the development region (i.e., $x \lesssim 4.7L$) contains the influence region of the source terms (i.e., $x \in [-0.3L, 0.3L]$). Hence, Fig. 7a shows the spectra in four locations in the development region: two inside of the influence region, $x = 0$ and $x = 0.15L$, and two outside of the influence region, $x = 0.5L$ and $x = L$. At $x = 0$, the energy spectrum is relatively narrow banded, with a maximum at wavelengths of the order of Λ_0. The spectrum becomes wider as x increases within the development region, progressively filling the high-wavenumber-end of the spectrum, as energy is cascaded down from larger scales to the dissipative range.

For the GT case, a different phenomenology is observed. First, the development length is now considerably larger ($x \lesssim 7.7L$), and hence the streamwise locations shown in Fig. 7b span a larger range. Second, the energy spectrum at the shortest distance considered (i.e., $x = L$, dashed curve in Fig. 7b) is already broad banded, with distinct peaks at wavelengths compatible with the grid geometry: one peak at $\kappa M \approx 2\pi$ compatible with the spacing between the rods ($\lambda \approx M$), and a second (smaller) peak at $\kappa M \approx 6\pi$ compatible with the width of the wakes of the rods ($\lambda \approx 1.35d$). Third, as x increases within the development region, these peaks are flattened (as the flow becomes more homogeneous, see discussion of Fig. 3), while the energy in the high-wavenumber-end of the spectrum decreases.

This points out that the process driving the development of the dissipative range in both cases is different: dissipation for the GT00 case, energy transfer for the ST1535-A case. This difference is significant, since it implies more stringent resolution requirements for the GT00 than for ST1535-A, as well as longer development regions (to homogenize the flow). Also, the fact that the energy spectrum of the ST1535-A case is narrow banded just downstream of the influence region appears as a feature that can be exploited in certain applications, like testing the effect of perturbations having a specific length-scale.

3.2. Free-stream turbulence control using ST

In this section we present the results of the parametric study using the ST approach. Departing from the baseline case, we have performed

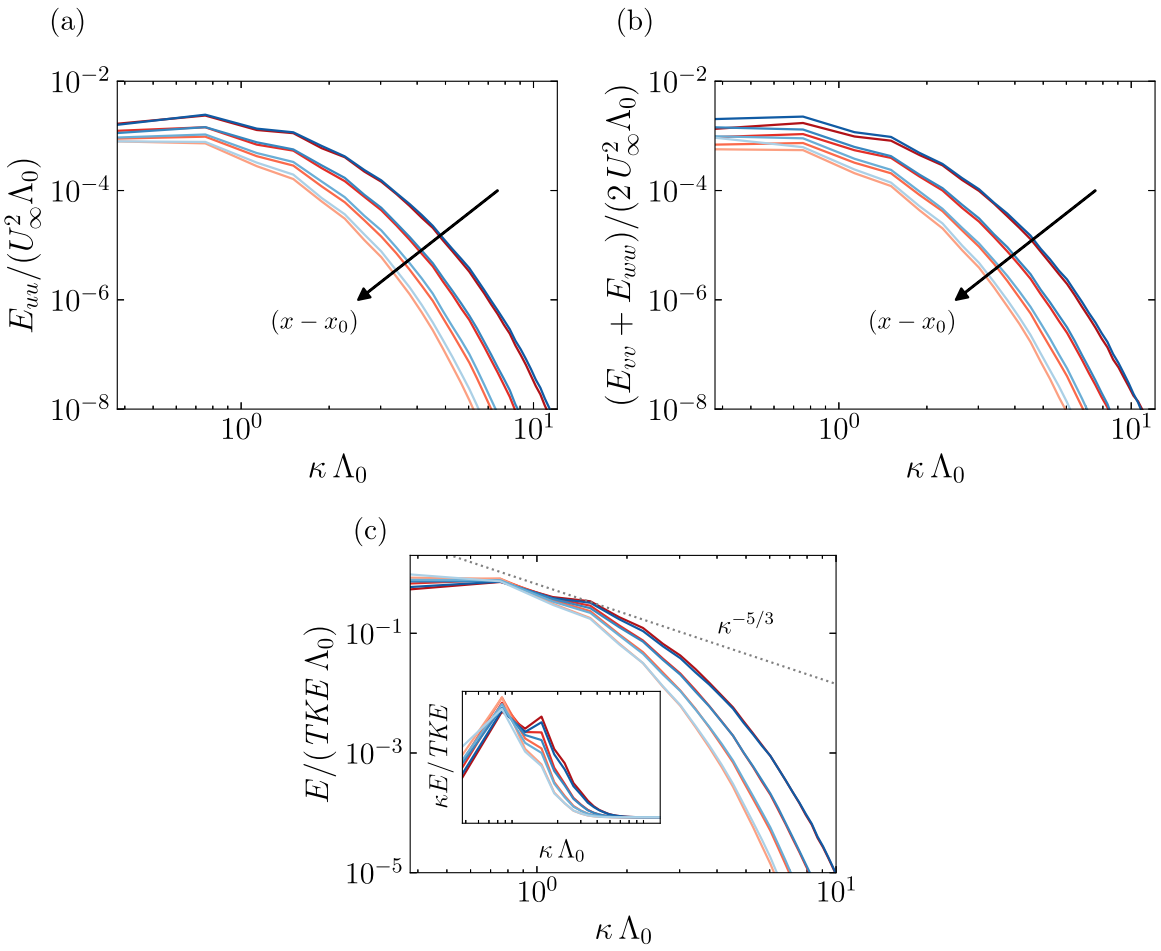

Fig. 6. (a) Streamwise and (b) transverse component energy spectrum for ST1535-A case (blue) and GT00 case (red), computed at different streamwise locations (increasing with brightness, $(x-x_0)/L = \{6, 9, 12, 15\}$), normalized with the incoming flow velocity U_∞ and ST input length-scale Λ_0. Note that in (b) we average between the v and w component. (c) Total energy spectrum at the same locations in (a,b), normalized with the turbulent kinetic energy TKE (at the corresponding location) and ST input length-scale Λ_0. The dotted line indicates the Kolmogorov scaling in the inertial subrange. The inset shows the same total energy spectrum pre-multiplied by the wavenumber magnitude.

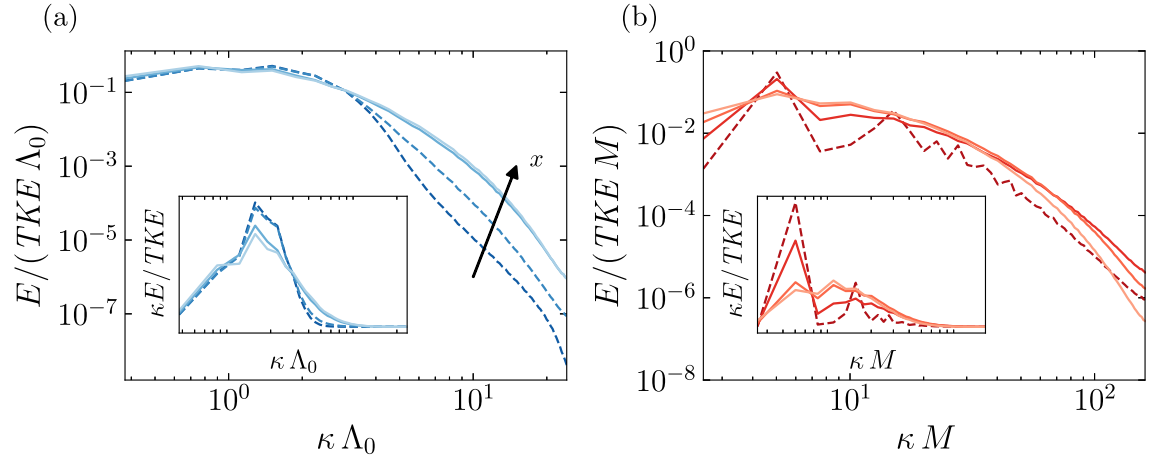

Fig. 7. (a) Total energy spectra inside and shortly after the region of influence in the ST1535-A case (blue curves, increasing with brightness $x/L = \{0, 0.15, 0.5, 1\}$, the first two inside the region of influence indicated by dashed lines). (b) Total energy spectra in the proximity of the passive grid in the GT00 case (red curves, increasing with brightness $x/L = \{1, 2, 3, 4\}$, the closest to the grid indicated by dashed line). Spectra are normalized with TKE and (a) ST input length-scale Λ_0 or (b) solid grid spacing $M \equiv L$. The insets report the pre-multiplied energy spectra.

additional simulations in which we have varied one of the input parameters (TI_0 or Λ_0) while keeping constant the other one. This allows us to assess the effect that these two parameters have on the main flow features. Such information is collected in Table 1, together with the power-law coefficients obtained using again the fitting procedure detailed in Appendix C.

Fig. 8 shows visualizations of instantaneous vortical structures of non-dimensional Q-criterion. The difference in the typical size of the

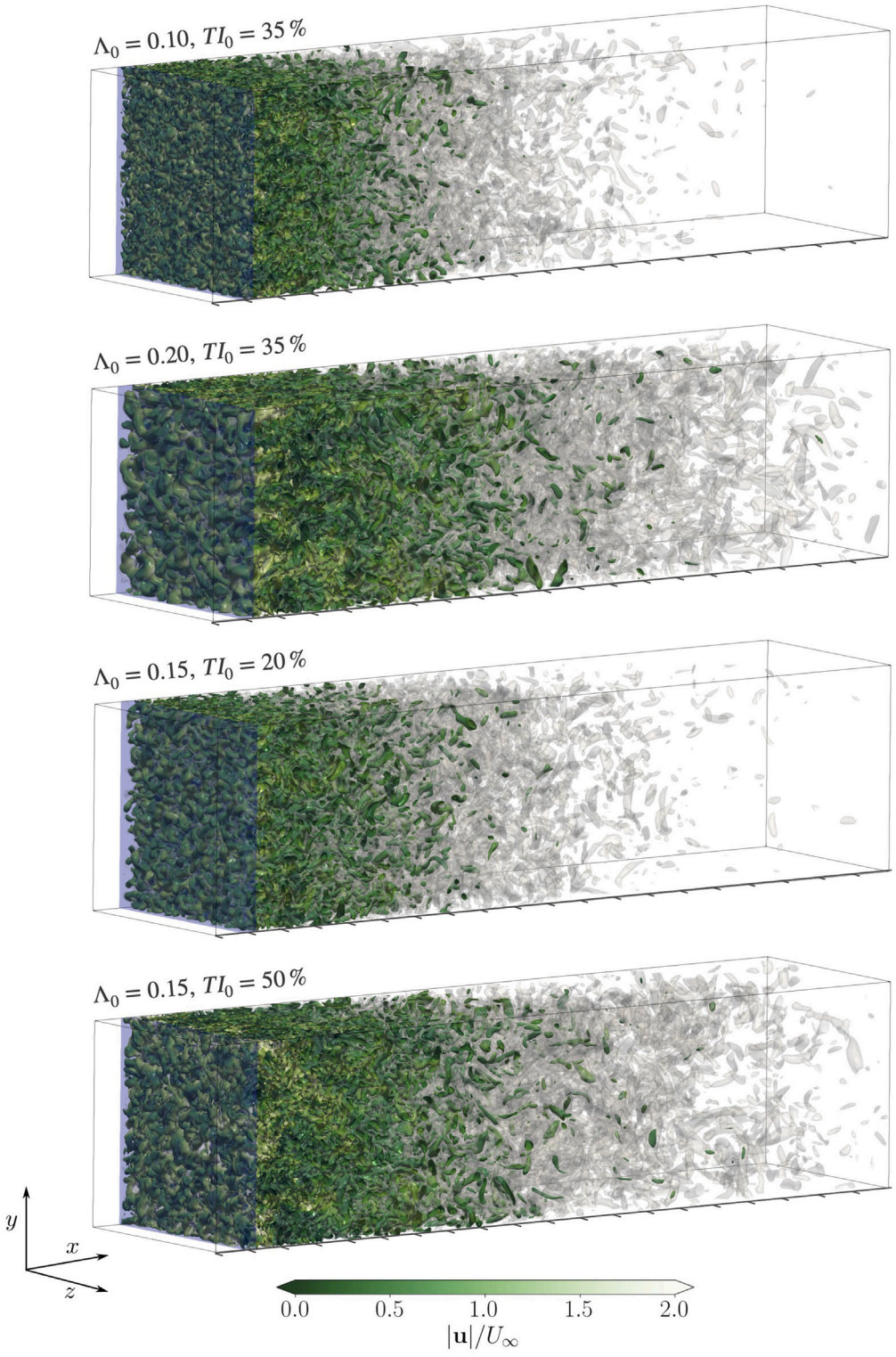

Fig. 8. Snapshots from the simulations performed with the ST approach, depicting the instantaneous vortical structures by means of isosurfaces at $QL^2/U_\infty^2 = [1, 0.2]$. The higher value is colored using the magnitude of the velocity, while the lower one is colored in white and with a lower opacity. The transparent blue box indicates the region of influence where the source term $\mathbf{f}_{st}$ is active. From top to bottom: case ST1035 ($\Lambda_0 = 0.10L, TI_0 = 35\%$), case ST2035 ($\Lambda_0 = 0.20L, TI_0 = 35\%$), case ST1520 ($\Lambda_0 = 0.15L, TI_0 = 20\%$) and case ST1550 ($\Lambda_0 = 0.15L, TI_0 = 50\%$).

flow structures generated over the whole injection region is particularly evident when comparing $\Lambda_0/L = 0.10$ and $\Lambda_0/L = 0.20$ cases. These two cases also showcase the effect of Λ_0 on the decay of the structures, showing that flow structures of both thresholds ($QL^2/U_\infty^2 = [1, 0.2]$) reach further downstream as we increase the input length-scale, Λ_0. In qualitative terms, a similar effect is observed when comparing $TI_0 = 20\%$ and $TI_0 = 50\%$ (at constant Λ_0), since we notice that the isosurfaces of Q-criterion are still present further downstream as we increase the input intensity TI_0. Zooming in the injection plane, one can also notice some differences between these last two cases. We

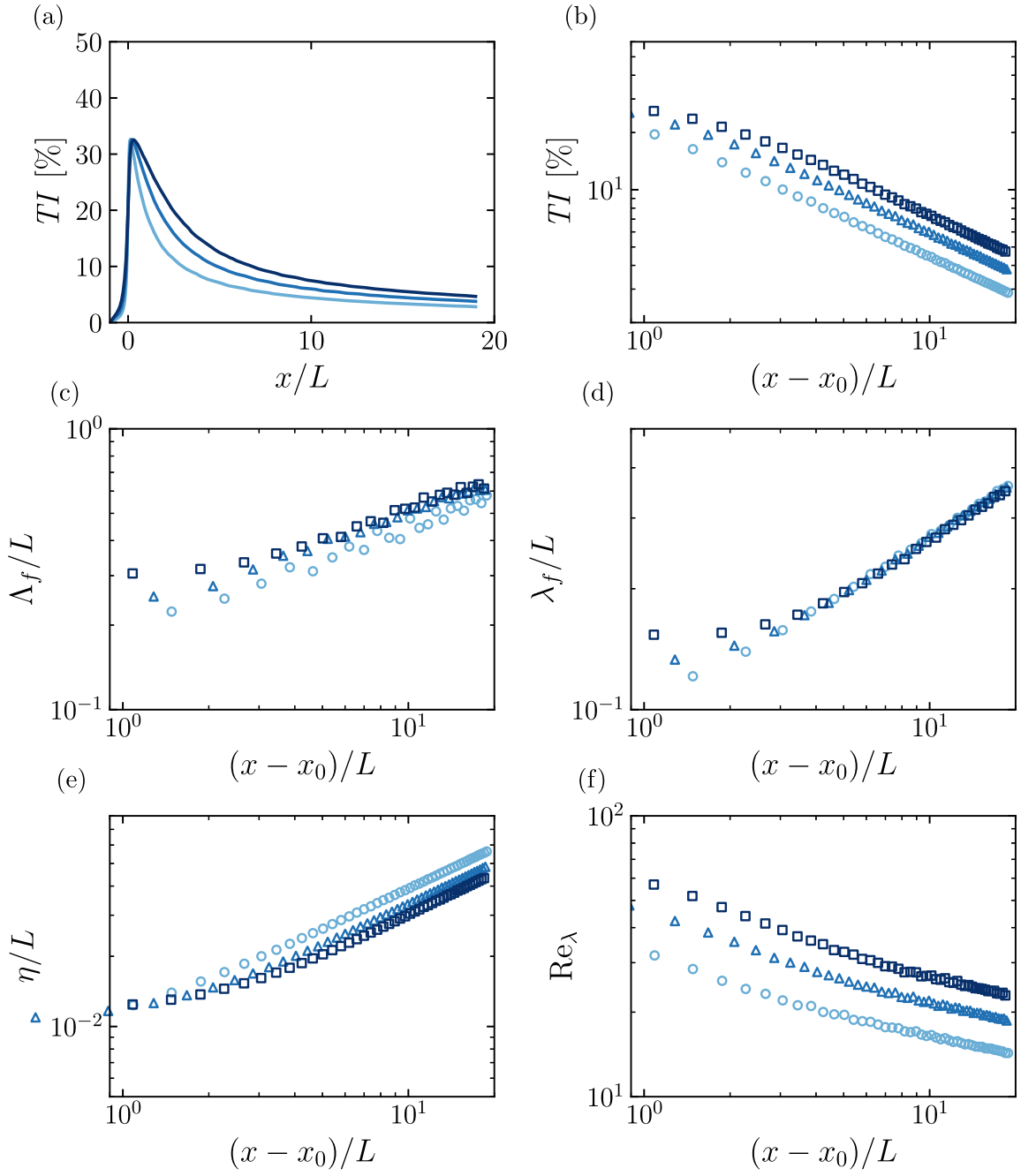

Fig. 9. Decay of turbulence intensity TI for cases at constant input intensity TI_0 (a,b). Characteristic length-scales and micro-scale Reynolds number at constant TI_0, as a function of $(x - x_0)$ (c-e). Note that all the panels are represented in logarithmic scale, except for panel (a), that is plotted in linear scale. Legend: case ST1035 ($\Lambda_0/L = 0.10$, light-blue), case ST1535-B ($\Lambda_0/L = 0.15$, blue), case ST2035 ($\Lambda_0/L = 0.20$, dark-blue).

can discern the presence of smaller eddies in case ST1550 than in case ST1520, which are probably related to the increased non-linearity of the flow as TI_0 increases.

In order to quantify the results, we focus first on the variation of the input length-scale Λ_0. Fig. 9a shows the decay of the turbulence intensity TI as a function of the streamwise coordinate. Although all three cases start from the same level of turbulence intensity, we can clearly observe that they quickly show a quantitatively different evolution moving downstream, with the slowest decay for the case with $\Lambda_0/L = 0.20$ and the fastest decay for the case with $\Lambda_0/L = 0.10$. Differences in decay rate are limited to a region very close to the injection plane: the power-law fitting procedure (computed as in the previous section) yields values for the virtual origin x_0 and power-law exponent n that are very close to the ST1535-B case, while the pre-multiplicative factor A grows as Λ_0 is increased (see Table 1). This is reflected in Fig. 9b, in which case ST2015 presents the highest turbulence intensity values among all the cases. In this figure, we can also see that the slopes n are practically the same for the three cases herein presented, meaning that their decay in the fully-developed region is very similar despite the existing differences in terms of initial length-scale. It can be identified, moreover, that the initial transient is different between these cases, apparently losing less energy in the case where larger scales are present ($\Lambda_0 = 0.20L$), compared to the other cases. Interestingly, the case with $\Lambda_0 = 0.20L$ also has a longer development region, adjusting to the power-law decay rate in Fig. 9b further downstream than the other two cases. This observation is confirmed by the values of x_i

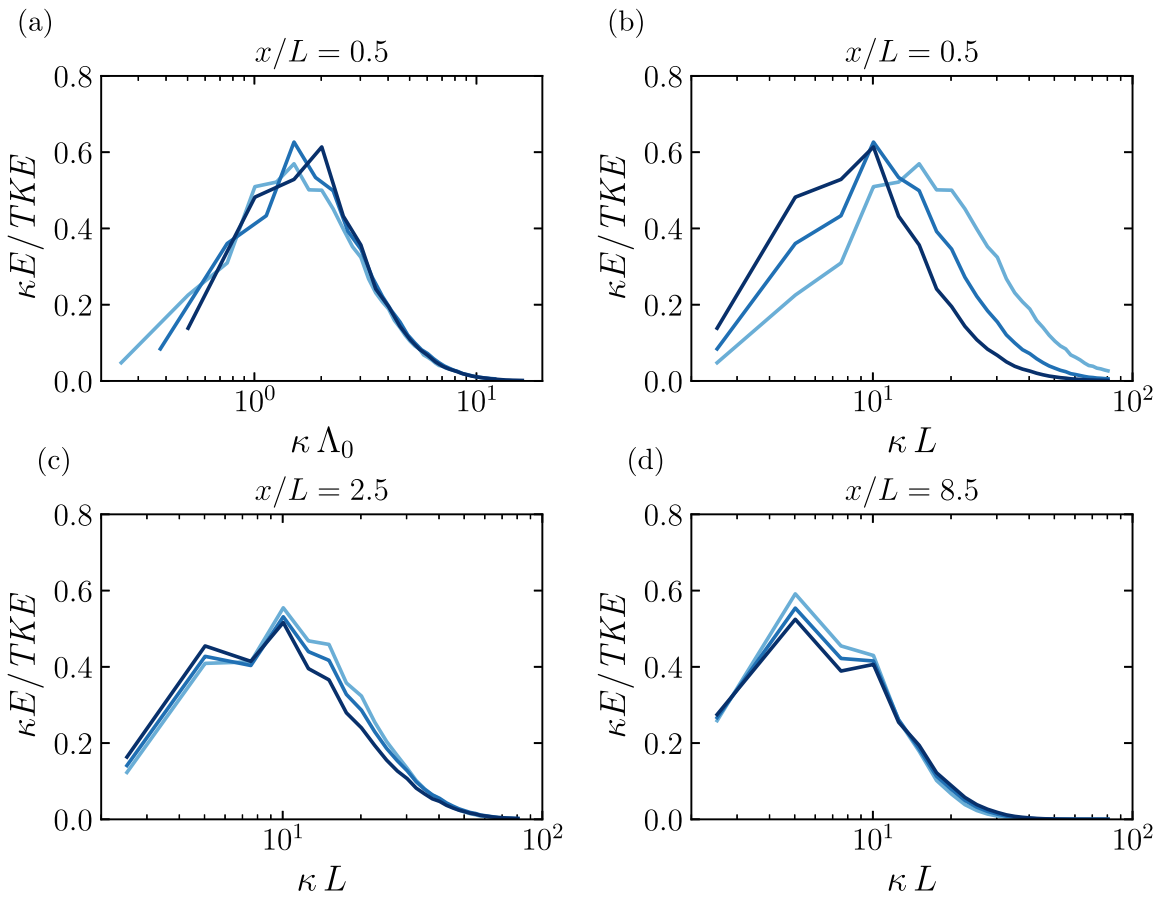

Fig. 10. Pre-multiplied spectra normalized with the turbulent kinetic energy, TKE, at different streamwise locations, normalizing κ with the input length-scale Λ_0 (a) or with the characteristic length of the problem L (b), both at $x = 0.5L$. Panels (c) and (d) show the same spectra against κL, at $x = 2.5L$ (c) and $x = 8.5L$ (d). Legend: case ST1035 ($\Lambda_0/L = 0.10$, light-blue), case ST1535-B ($\Lambda_0/L = 0.15$, blue), case ST2035 ($\Lambda_0/L = 0.20$, dark-blue).

provided in Table 1, and it can be linked to the characteristic time scale of the largest eddies injected in the flow, $t_\Lambda = \Lambda_0/(TI_0U_\infty)$. The development region can be understood as the region where the large scale eddies interact to each other to generate the energy cascade, while they are advected downstream by the free-stream velocity U_∞. The time required for these interactions to take place scales with t_Λ, the eddy turn-over time. In that sense, the length of the development region x_i should be proportional to $U_\infty t_\Lambda = \Lambda_0/TI_0$, which is consistent with the data provided in Table 1, increased with Λ_0 for constant TI_0. Note that the dependence of the development region's length with Λ_0 is partially taken into account by x_0 (which also increases with Λ_0), but not by n or A, which describe the decay rate in the region in which the flow is fully developed.

To deepen our analysis we now turn our attention to the streamwise evolution of the characteristic length-scales of the flow (Fig. 9c–f), and to the streamwise evolution of the premultiplied energy spectra (Fig. 10). The length-scales shown in Fig. 9c-f are the longitudinal integral length-scale Λ_f, the longitudinal Taylor scale λ_f and the Kolmogorov scale η, together with the micro-scale Reynolds number Re_λ. If we first consider the evolution of the integral length-scale (Fig. 9c) and the Taylor scale (Fig. 9d), it is clear that these length-scales are unambiguously different in the vicinity of the injection region for the three values of Λ_0 considered here. Conversely, these length-scales get closer to each other as the flow develops downstream, with a perfect collapse of λ_f/L and an approximate collapse of Λ_f/L for all Λ_0's in the fully developed region. The differences in Λ_f and λ_f close to the influence region of the ST can also be observed in Fig. 10a–b, which show the energy spectrum at $x/L = 0.5$. Decreasing Λ_0 shifts the energy spectrum towards smaller scales (i.e., higher wavenumbers), as shown in Fig. 10b. But when the wavenumber κ is normalized with Λ_0, as done in Fig. 10a, the spectral distribution of energy is almost the same for the three values of Λ_0, with the energy peak centered close to $\kappa\Lambda_0 \simeq 1$.

The growth of Λ_f and λ_f with x observed in Fig. 9c–d, and the convergence of the Λ_f's and λ_f's as x increases, is also apparent when comparing the spectrum at different streamwise locations as in Fig. 10. The figure shows that the spectrum gets shifted towards smaller wavenumbers (i.e., larger length-scales) as x increases. Moreover, the differences between the spectral energy distribution for different Λ_0's become smaller as x increases (compare Fig. 10b, c and d). This suggests that once the flow is fully-developed, it becomes memory-less with respect to the initial transient (governed by Λ_0 in these cases).

Regarding the Kolmogorov length-scale η, shown in Fig. 9e, our results reveal a streamwise development that is almost the opposite to the one corresponding to the Λ_f and λ_f: no effect of Λ_0 on η close to the influence region, and lack of collapse of η further downstream for different Λ_0's. Moreover, in the decaying region η becomes smaller as Λ_0 increases. This is likely a consequence of the effect of Λ_0 on the TI at a given $(x-x_0)/L$. Larger values of TI (at similar values of Λ_f) implies more energy cascading downscale, which requires a smaller value of the Kolmogorov length-scale to dissipate that downscale energy flux. This is also reflected in the decay of the micro-scale Reynolds number $\mathrm{Re}_\lambda \equiv u_{\mathrm{rms}}\lambda_f/\nu$ presented in Fig. 9f, showing higher values for Λ_0 =

$0.20L$ compared to the other two cases, indicative of a larger separation of scales between the energy-containing and dissipative ranges. It is important to emphasize that the effect of Λ_0 in the Kolmogorov length-scale and the scale separation in the fully developed region is driven by the turbulence intensity $TI(x)$, which in turn is controlled by effect of Λ_0 in the dynamics of the development region.

Turning now our attention to the cases where we keep constant the input scale $\Lambda_0 = 0.15$ and vary the input intensity (TI_0={20%,35%,50%}), it becomes clear that this change has a direct effect on the evolution of the computed turbulence intensity TI, as shown in Fig. 11a. The most intense case ($TI_0 = 50\%$, dark red) has larger values of TI at a given streamwise position than the other two cases. Conversely, the most intense cases lose more turbulent kinetic energy in the development region in absolute terms, something that can be inferred from the figure as well.

In a similar fashion as before, we can represent TI in logarithmic scale and perform the power-law fit as in Lavoie et al. [48], yielding A, n and x_0. As reported in Table 1, we obtain almost identical virtual origins x_0 for cases ST1535-B and ST1550. On the other hand, we find that the virtual origin x_0 is considerably decreased for the lowermost input intensity case (ST1520, $TI_0 = 20\%$). Besides, Fig. 11b shows that the end of the development region for these cases (i.e., the point where TI starts the power-law decay) is coherent with the values provided by x_i and x_0 in Table 1, featuring a development distance that is longer for case ST1520 than for case ST1550, with the baseline case ST1535-B in between them. This implies that the development length becomes shorter as TI_0 increases, in agreement with the scaling based on the eddy turn-over time $t_\Lambda = \Lambda_0/(TI_0 U_\infty)$ described in the previous paragraphs: at constant Λ_0, larger input intensity TI_0 translates into a shorter eddy turn-over time, enhancing the non-linear interactions taking place in the development region and thus shortening the length required by the flow to reach a fully-developed state. In passing, the effect of TI_0 also results in a relatively large variation of the decay exponent n (see Table 1) with a relatively noticeable lack of parallelism between the different curves shown in Fig. 11b. For the pre-multiplicative factor A, on the other hand, the differences are limited, but still present and consistent.

Replicating the analysis performed before for the cases at constant TI_0, we find that the evolution of the longitudinal integral length-scale is relatively insensitive to the value of TI_0, with an approximate collapse of Λ_f in Fig. 11c. A better collapse is observed for the longitudinal Taylor length-scale, not shown here. The collapse of Λ_f for all TI_0's can also be observed in the streamwise evolution of the pre-multiplied spectra, shown in figure Fig. 12. In order to contrast these results, we present in Fig. 12 the pre-multiplied spectra normalized with the turbulent kinetic energy, TKE, at different streamwise locations ($x/L = \{0.5, 2.5, 8.5\}$). As expected, the spectra at $x/L = 0.5$ shown in Fig. 12a exhibit an energy peak centered around the same wavenumber for the three values of TI_0 considered. However, the high-wavenumber tail of the premultiplied spectra becomes longer as TI_0 increases (i.e., the smallest scales become smaller), suggesting stronger non-linear interactions (and smaller Kolmogorov length-scale) for the highest intensity case ($TI_0 = 50\%$, dark red). This is consistent with the values of Re_λ reported in Fig. 11d.

When the premultiplied spectra of the three cases with different TI_0 are compared further downstream (Fig. 12b–c), we observe the same qualitative behavior discussed for the spectra of the cases with different Λ_0: the spectra for different TI_0 gradually collapse as x increases, shifting towards smaller wavenumbers (i.e., larger length-scales).

To close this section, we report negligible effect of both Λ_0 and TI_0 on the anisotropy of the large scales R (defined in Section 2.4). For the five cases discussed in this section, the anisotropy index remains bounded between $0.95 < R < 1.05$, comparable to the range of variation of R for ST1535-A in Fig. 4b.

4. Conclusions

In this work, we have investigated the generation of decaying turbulence with desirable and controllable properties using synthetic turbulence (ST) at a relatively low Reynolds number of Re = 1000 by means of direct numerical simulations. Specifically, we have considered the synthetic turbulence (ST) approach using the digital filtering technique originally proposed by Klein et al. [33] and later extended by Kempf et al. [38] and Schmidt and Breuer [39].

Firstly, we have compared the results of the ST approach with those of a grid-induced turbulence (GT), reproducing numerically the typical setup adopted in wind tunnels. A first observation is the different development length along the streamwise direction to achieve a homogeneous turbulent flow. For a quantitative comparison, we have accounted for this effect in terms of the virtual origin x_0 obtained by fitting the turbulent kinetic energy TKE to the well-known power law, Eq. (4), and the approximate streamwise coordinate where the power-law decay begins, x_i. Both metrics show that the development region for the ST case is significantly shorter than that for the GT case. Another remarkable difference is found for the large-scale anisotropy, with the ST having an almost isotropic behavior while the GT showing a considerable degree of anisotropy (at least for the considered Reynolds number and geometrical configuration). Moreover, we have compared the streamwise evolution of the characteristic length-scales and the micro-scale Reynolds number, showing an overall good mutual resemblance. Finally, the analysis of the turbulent energy spectrum where the flow is developed is consistent with the typical phenomenology of decaying turbulence. However, focusing on the ST approach and in the vicinity of the region of influence, the spectrum looks relatively narrow banded and this property can be exploited, e.g., to test the aerodynamic response to perturbations of a specific length-scale.

In the second part of the work, we have performed a parametric study over the ST input parameters, i.e., nominal turbulence intensity and integral length-scale (using the ST1535 case as the baseline). Focusing first on the streamwise evolution of the turbulence intensity TI, a relatively strong dependence with the input parameters appears, with higher intensities as both input parameters are increased. On the other hand, we have identified some differences in terms of the development length, found to be shorter for the case with $\Lambda_0 = 0.10L$ than for case with $\Lambda_0 = 0.20L$, i.e., exhibiting in the former a fully-developed flow at an earlier streamwise location. The contrary is observed when we vary the input intensity TI_0, for which the case with the highest intensity ($TI_0 = 50\%$) shows a shorter development length than the case with $TI_0 = 20\%$. We suggest that these trends are consistent and possibly linked to the differences in the eddy turn-over time between these cases, which suggests a development length proportional to Λ_0/TI. Finally, we have assessed the relative separation of scales between the cases by focusing on the characteristic length-scales and the micro-scale Reynolds number as a function of the streamwise coordinate, together with the spectral energy distribution at different locations. We have reported a higher scale separation for cases ST2035 and ST1550 (highest Λ_0 and TI_0, respectively), as well as an evolution of the energy spectrum consistent with the phenomenology of decaying turbulence: while presenting some initial differences in the development region, the spectra shift progressively towards the lower wavenumbers as x is increased, substantially becoming memory-less with respect to the initial transient.

From a practical point of view, the results of our study suggest two possible uses for the ST to perturb a uniform free stream. If the application requires a narrow-banded perturbation (i.e., in terms of spatial and/or temporal wavenumbers), the injection plane of the ST must be placed relatively close to where the perturbations are needed, at distances $< 6\Lambda_0/TI$. On the other hand, if the application requires turbulence-like energy spectrum (i.e., like the one observed in freely-decaying turbulence), the injection plane of the ST must be placed

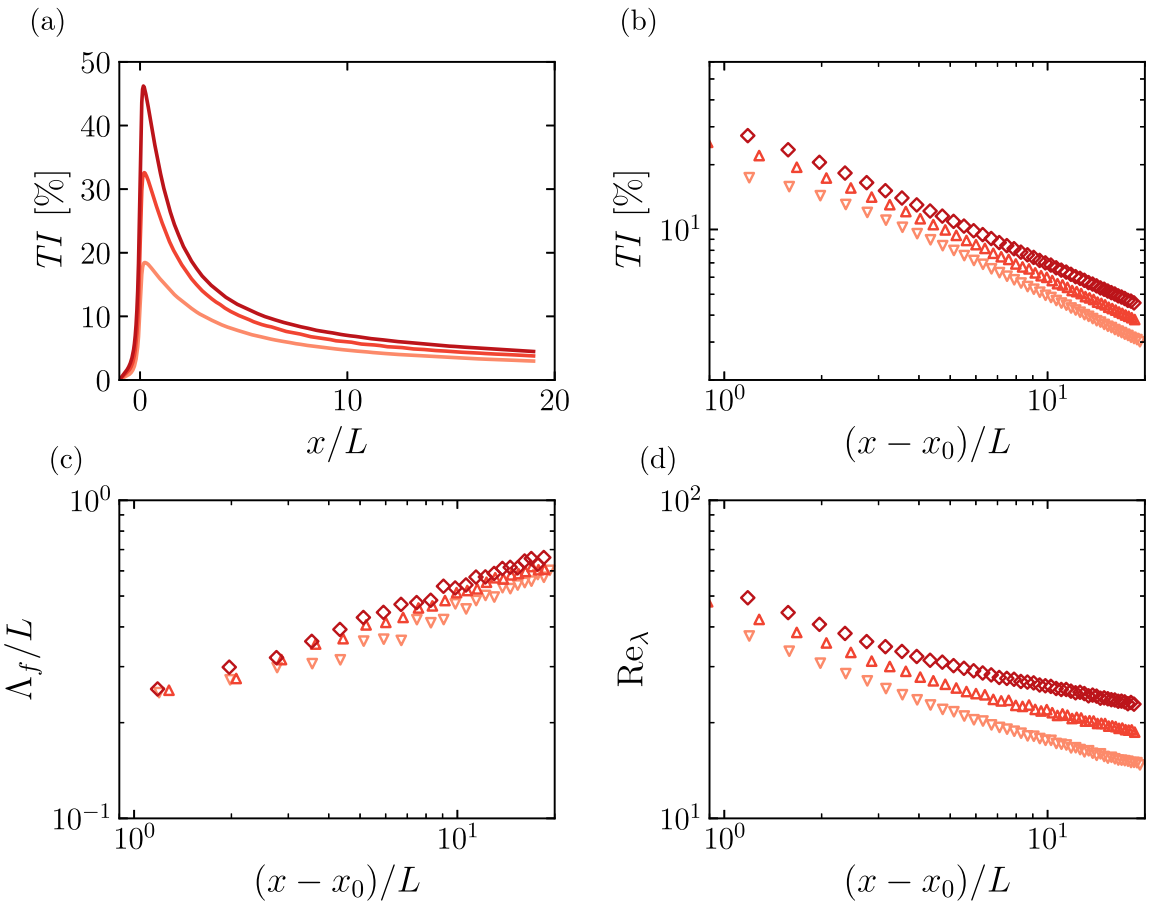

Fig. 11. Decay of turbulence intensity TI for cases at constant input length-scale Λ_0 (a,b). Longitudinal integral length-scale (c) and micro-scale Reynolds number (d) at constant TI_0, as a function of $(x - x_0)$. Note that all the panels are represented in logarithmic scale, except for panel (a), that is plotted in linear scale. Legend: case ST1520 ($TI_0 = 20\%$, light-red), case ST1535-B ($TI_0 = 35\%$, red), case ST1550 ($TI_0 = 50\%$, dark-red).

further away, at distances $\gtrsim 6\Lambda_0/TI$. Note that in the former case, the effective intensity and wavelength of the perturbations will be of the same order of magnitude as Λ_0 and TI_0, while in the latter the power-law decay must be taken into account to estimate the required TI and Λ of the ST.

CRediT authorship contribution statement

J.M. Catalán: Writing – original draft, Visualization, Validation, Methodology, Investigation, Formal analysis, Data curation, Conceptualization. **S. Olivieri:** Writing – review & editing, Writing – original draft, Validation, Methodology, Investigation, Funding acquisition, Formal analysis, Data curation, Conceptualization. **M. García-Villalba:** Writing – review & editing, Supervision, Methodology, Investigation, Funding acquisition, Conceptualization. **O. Flores:** Writing – review & editing, Supervision, Methodology, Investigation, Funding acquisition, Conceptualization.

Declaration of competing interest

The authors declare that they have no known competing financial interests or personal relationships that could have appeared to influence the work reported in this paper.

Data availability

Data will be made available on request.

Acknowledgments

The authors thankfully acknowledge the computer resources at Picasso and the technical support provided by the Supercomputing and Bioinnovation Center (SCBI) of the University of Malaga (RES-IM-2023-1-0021 and RES-IM-2023-2-0017). This work is supported by grant PID2022-142135NA-I00 by MCIN/AEI/10.13039/501100011033 and grants FJC2021-047652-I and TED2021-131282B-I00 by MCIN/AEI/10.13039/501100011033 and European Union NextGenerationEU/PRTR. Funding for APC: Universidad Carlos III de Madrid (Agreement CRUE-Madroño 2024).

Appendix A. Generation of perturbation velocity using digital filters

We use the digital filtering approach of Kempf et al. [38] to generate the fluctuation velocity field $\mathbf{u}'(t, y, z)$. This is achieved by filtering a set of random numbers $r(i', j, k)$, for each velocity component u', v' and w', as follows:

$$h_1(j,k) = \sum_{i'=-N_x}^{N_x} b_x(i') \cdot r(i', j, k), \tag{6a}$$

$$h_2(j,k) = \sum_{j'=-N_y}^{N_y} b_y(j') \cdot h_1(j + j', k), \tag{6b}$$

$$u'(j,k) = \sum_{k'=-N_z}^{N_z} b_z(k') \cdot h_2(j, k + k'), \tag{6c}$$

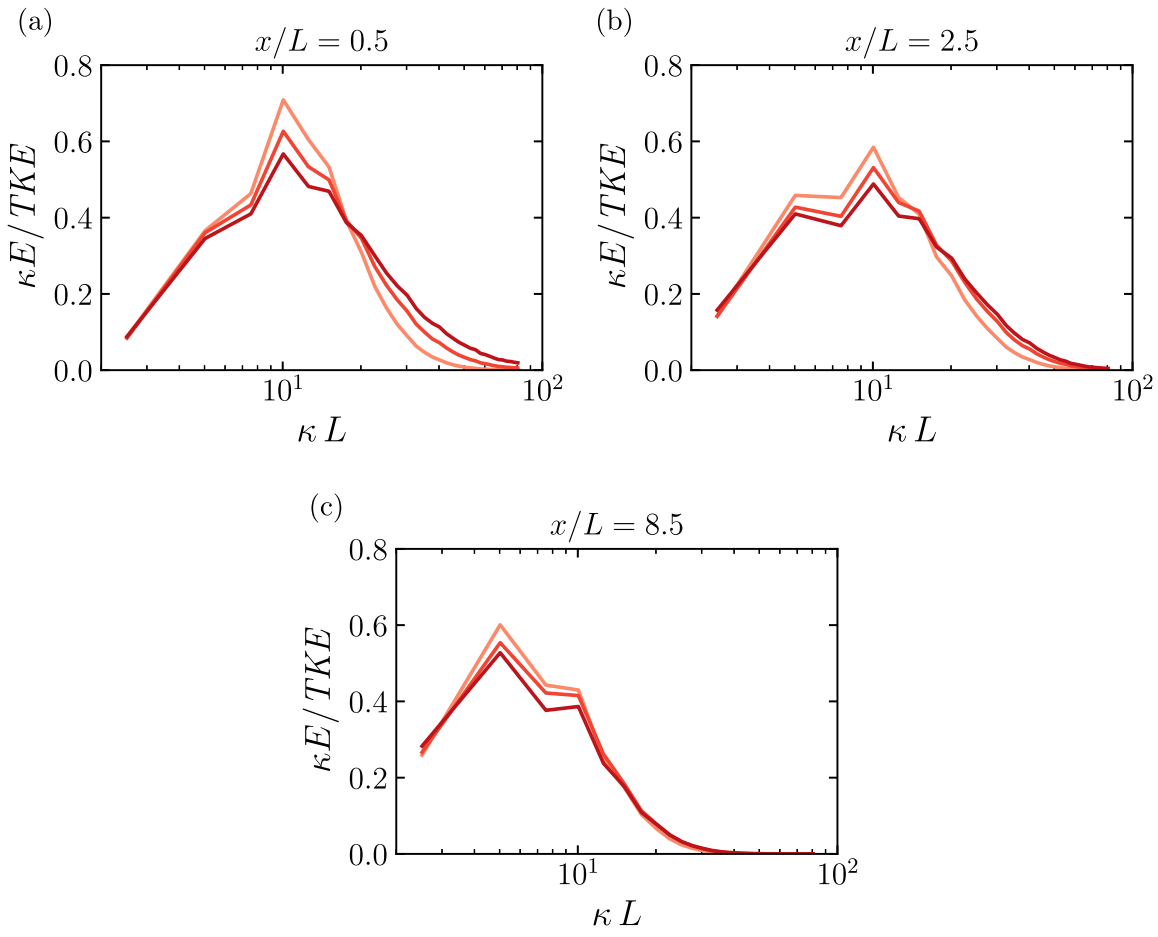

Fig. 12. Pre-multiplied spectra normalized with the turbulent kinetic energy, TKE, at different streamwise locations, normalizing κ with the characteristic length of the problem L. Locations: $x = 0.5L$ (a), $x = 2.5L$ (b) and $x = 8.5L$ (c). Legend: case ST1520 ($TI_0 = 20\%$, light-red), case ST1535-B ($TI_0 = 35\%$, red), case ST1550 ($TI_0 = 50\%$, dark-red).

where (j, k) are the indices of the nodes in the ST injection plane, ranging from 1 to the number of nodes in the y and z directions, M_y and M_z, respectively (note that $M_y \times M_z$ denotes the dimensions of the computational grid in the inflow plane). Additionally, (i', j', k') are the indices over the filter supports N_x, N_y and N_z ($i' \in [-N_x, N_x]$, $j' \in [-N_y, N_y]$, $k' \in [-N_z, N_z]$), where the filter supports are intrinsically related to the length and time scales of the desired fluctuation velocity field, as shown below. Finally, (b_x, b_y, b_z) are the filter coefficients, defined below in (7). Some intermediate buffers, h_1 and h_2, are created along the filtering process and contain the information of the filtered random numbers at intermediate steps. The filter operation is performed by axis, first along x (6a), then along y (6b) and finally along z (6c).

To fulfill the periodicity in the lateral boundaries (y, z) and thus produce a fluctuation velocity $u'(j, k)$ that is fully compatible with the boundary conditions, the set of random numbers $r(i', j, k)$ is also made periodic along these directions. These operations are done for each velocity component.

For each axis $\alpha = \{x, y, z\}$, the filter coefficients b_α are computed as detailed in Klein et al. [33]:

$$b_\alpha(k) \approx \tilde{b}_\alpha(k) \Big/ \left(\sum_{j=-N_\alpha}^{N_\alpha} \tilde{b}_\alpha^2(j) \right)^{1/2} \quad \text{with} \quad \tilde{b}_\alpha(k) = \exp\left(-\frac{\pi k^2}{2 n_\alpha^2} \right), \tag{7}$$

with n_α being the number of points per length-scale $n_\alpha = \Lambda_0/\Delta\alpha$, the filter support $N_\alpha \geq 2n_\alpha$ and $k \in [-N_\alpha, N_\alpha]$. A Gaussian auto-correlation function is assumed, such that the integral length-scale of the fluctuation velocity field generated is equal to the input length-scale Λ_0. For completeness, the number of points per length-scale and thus the filter supports are calculated in this work as:

$$n_x = T_0/\Delta t \equiv \Lambda_0/(U_\infty \Delta t), \qquad N_x = 2n_x \tag{8a}$$

$$n_y = \Lambda_0/\Delta y, \qquad N_y = 2n_y \tag{8b}$$

$$n_z = \Lambda_0/\Delta z, \qquad N_z = 2n_z \tag{8c}$$

where the time scale T_0 and the length-scale in the streamwise direction Λ_0 are related through Taylor's Hypothesis [47], as introduced in section Section 2.1. This results in a fluctuation velocity plane that is then injected in a three-dimensional region of the domain using a Gaussian bell-shape, as described in Section 2.1, fulfilling a correlation length that is the same in all directions (isotropic velocity field). Throughout this process, a sequential update of $r(i', j, k)$ is performed at each time step to introduce new randomness in the generated data [33].

Appendix B. Grid convergence analysis

In this section, we assess the influence of the numerical resolution on the presented results. For this purpose, we have considered the two cases analyzed in Section 3.1, i.e., the ST1535 case (where $\Lambda_0/L = 0.15$ and $TI_0 = 35\%$) and the GT00 case. We have run the two simulations on a finer grid where the spatial resolution is $\Delta/L \approx 0.02$ and a coarser grid where $\Delta/L \approx 0.04$. Note that the timestep used for the finer grid is half of that used for the coarser grid, in order to keep the same maximum CFL ≈ 0.3.

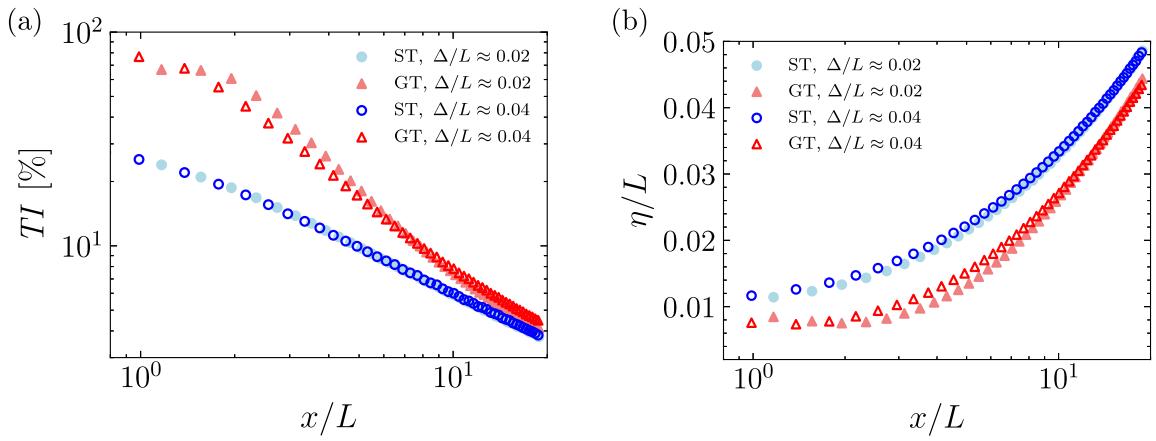

Fig. 13. Grid convergence study on bulk properties of the turbulent flow in the ST1535 (blue circles) and GT00 case (red triangles), reported as a function of the streamwise coordinate: (a) turbulence intensity; (b) Kolmogorov length-scale. Filled and empty symbols refer to the higher ($\Delta/L \approx 0.02$) and lower resolution ($\Delta/L \approx 0.04$), respectively.

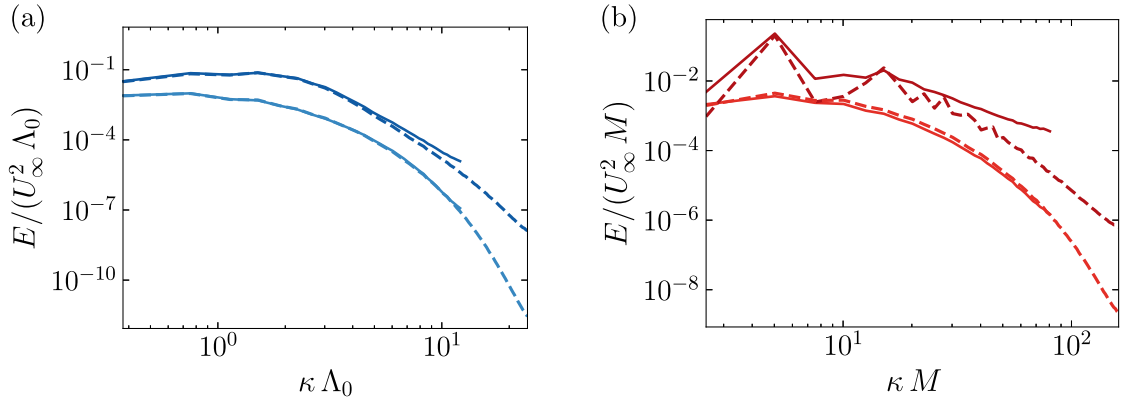

Fig. 14. Grid convergence study on the spectral energy distribution of (a) ST1535 case (dark at $x/L = 0.15$ and light at $x/L = 5$) and (b) GT00 case (dark at $x/L = 1$ and light at $x/L = 5$). Dashed and solid lines indicate the results for the higher ($\Delta/L \approx 0.02$) and lower resolution ($\Delta/L \approx 0.04$), respectively.

Fig. 13 shows the streamwise evolution of two relevant quantities in the resulting turbulent flows for both cases and considered resolutions. For the turbulence intensity (Fig. 13a), a certain difference can be noticed for the GT00 case in the earlier development region, arguably because of the large gradients involved in the shedding around the solid grid that are better resolved in the refined case. When focusing on the developed region (i.e., $x/L \gtrsim 3$), however, a better resemblance between the lower and higher resolution can be observed. The difference becomes eventually negligible while moving sufficiently downstream. For the ST1535 case, in comparison, the differences are essentially negligible. A similar outcome is obtained when looking at the Kolmogorov length-scale (Fig. 13b), with a relatively higher sensitivity to the resolution for the GT than for the ST case. Note that, while the turbulence intensity is a large-scale observable accounting for the entity of the velocity perturbations, the Kolmogorov length-scale is representative for the energy dissipation, thus complementing the characterization of the turbulent flow.

In Fig. 14, we compare the total energy spectra obtained with the higher (dashed line) and lower (solid line) resolution at two representative streamwise locations. For the ST1535 case (Fig. 14a), we consider the locations $x = 0.15L$ inside the region of influence (dark blue curves) and $x = 5L$ where the flow is properly developed (light blue). Overall, only minimal differences can be appreciated between the coarser and finer grid. For the GT00 case (Fig. 14b), we focus on $x = L$ (dark red) and $x = 5L$ (light red) as well. For the former location, some differences can be observed that are consistent with those already shown in Fig. 13. On the other hand, the sensitivity to the resolution is negligible when moving downstream to the latter location.

Appendix C. Power-law decay fitting procedure

This appendix includes additional information on how we have determined the coefficients of the power-law Eq. (4): A, n and x_0. To obtain them we have followed, in particular, the method proposed by Lavoie et al. [48]; note however that other techniques have proposed, e.g., in Krogstad and Davidson [60],Hearst and Lavoie [61]. The adopted procedure essentially consists in repeatedly fitting the power-law decay for the turbulent kinetic energy (or, equivalently, for the turbulence intensity) imposing different values of the virtual origin x_0 (so that only two coefficients, n and A, are involved in the actual fit) and different starting locations x_i of the range over which the power-law decay is considered to hold. As a result, each fit corresponds to a point in the plots shown by Figs. 15 and 16 for the obtained values of n and A, respectively.

To select the best combination of A, n and x_0 (along with x_i) as accurately as possible, we proceed as follows. Firstly, we choose the virtual origin x_0 by looking for the curve showing the longest plateau of the decay exponent n in Fig. 15 (note that the fits with same virtual origin x_0 have the same color). Once the branch with the longest plateau has been identified (and thus the virtual origin x_0), we select the minimum point in such branch before it deviates from the plateau by more than 0.5%, as proposed by Lavoie et al. [48]. This allows us to directly obtain the value of the power-law exponent n, which is the vertical coordinate of that point. Lastly, with such point identified it is also possible, by inspecting Fig. 16, to obtain the value of the multiplicative factor A.

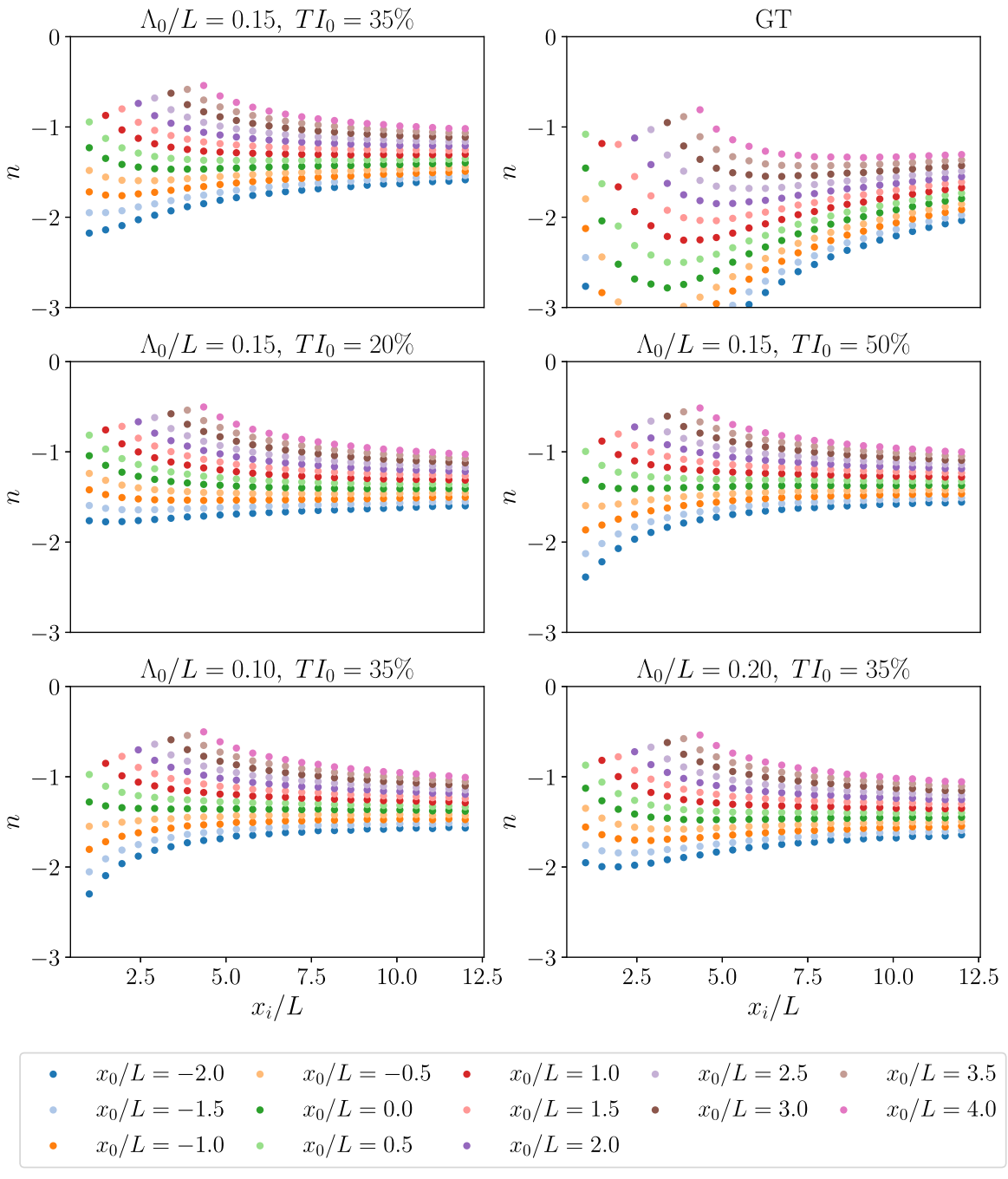

Fig. 15. Results of the performed power-law fit for the decay exponent n.

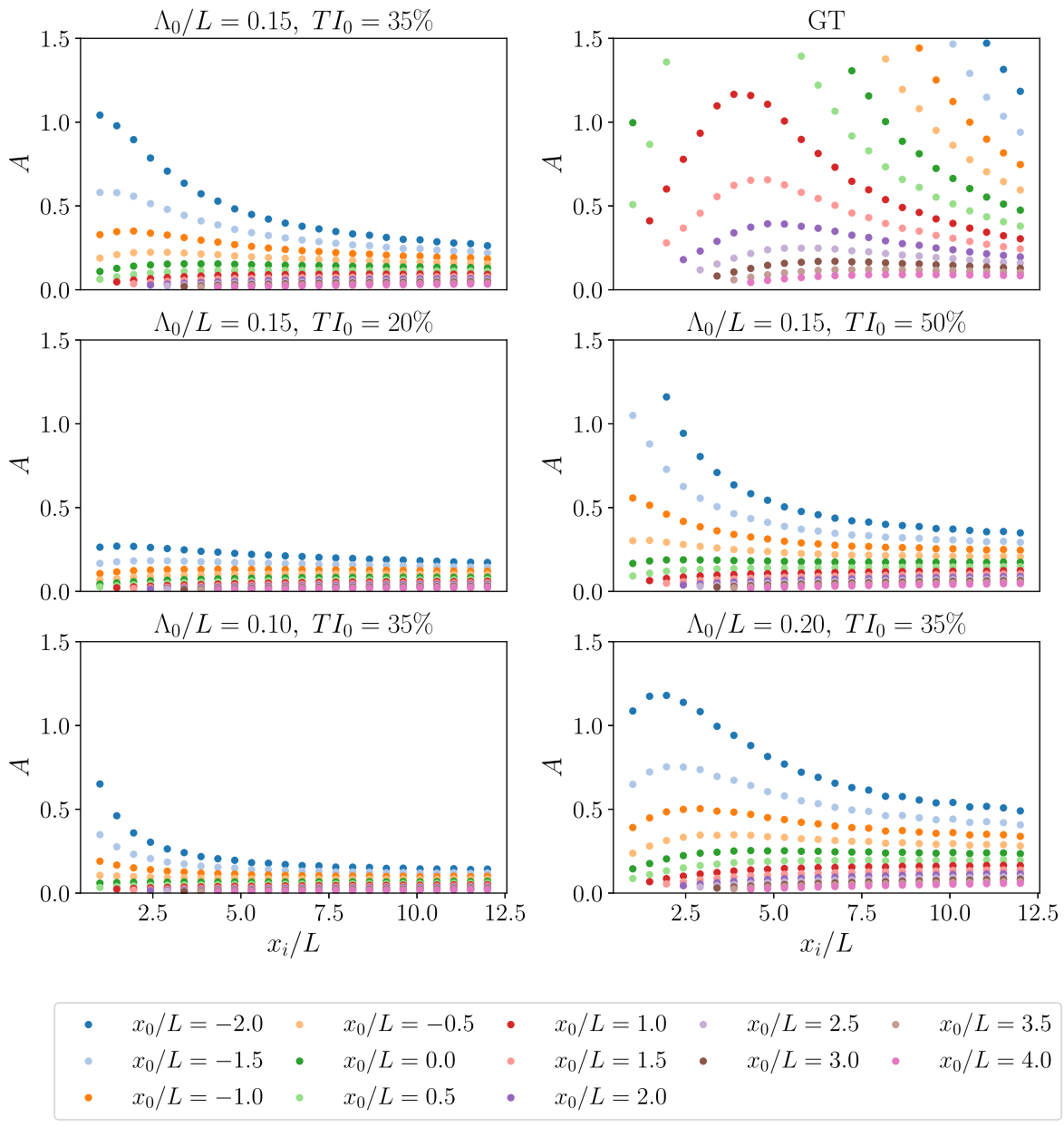

Fig. 16. Results of the performed power-law fit for the multiplicative factor A.

References

[1] Bearman P, Morel T. Effect of free stream turbulence on the flow around bluff bodies. Prog Aerosp Sci 1983;20(2–3):97–123.

[2] So R, Wang X, Xie W-C, Zhu J. Free-stream turbulence effects on vortex-induced vibration and flow-induced force of an elastic cylinder. J Fluid Struct 2008;24(4):481–95.

[3] Li M, Li Q, Shi H, Li M. Effects of free-stream turbulence on the near wake flow and aerodynamic forces of a square cylinder. J Fluids Struct 2022;114:103748.

[4] Huang RF, Lee HW. Effects of freestream turbulence on wing-surface flow and aerodynamic performance. J Aircr 1999;36(6):965–72.

[5] Jin Y, Ji S, Chamorro LP. Spectral energy cascade of body rotations and oscillations under turbulence. Phys Rev E 2016;94(6):063105.

[6] Leib S, Wundrow DW, Goldstein M. Effect of free-stream turbulence and other vortical disturbances on a laminar boundary layer. J Fluid Mech 1999;380:169–203.

[7] Brandt L, Schlatter P, Henningson DS. Transition in boundary layers subject to free-stream turbulence. J Fluid Mech 2004;517:167–98.

[8] Fransson JHM, Matsubara M, Alfredsson PH. Transition induced by free-stream turbulence. J Fluid Mech 2005;527:1–25.

[9] Dogan E, Hanson RE, Ganapathisubramani B. Interactions of large-scale free-stream turbulence with turbulent boundary layers. J Fluid Mech 2016;802:79–107.

[10] Shyy W, Aono H, Chimakurthi S, Trizila P, Kang C-K, Cesnik C, et al. Recent progress in flapping wing aerodynamics and aeroelasticity. Prog Aerosp Sci 2010;46(7):284–327.

[11] Haider N, Shahzad A, Qadri MNM, Shah SIA. Recent progress in flapping wings for micro aerial vehicle applications. Proc Inst Mech Eng C J Mech Eng Sci 2021;235(2):245–64.

[12] Bourhis M, Pereira M, Ravelet F. Experimental investigation of the effect of blade solidity on micro-scale and low tip-speed ratio wind turbines. Exp Therm Fluid Sci 2023;140:110745.

[13] Lysenko DA. Free stream turbulence intensity effects on the flow over a circular cylinder at Re=3900: Bifurcation, attractors and Lyapunov metric. Ocean Eng 2023;287:115787.

[14] Watkins S, Milbank J, Loxton BJ, Melbourne WH. Atmospheric winds and their implications for microair vehicles. AIAA J 2006;44(11):2591–600.

[15] Martínez-Muriel C, Flores O. Analysis of vortical gust impact on airfoils at low Reynolds number. J Fluid Struct 2020;99:103138.

[16] Mohamed A, Clothier R, Watkins S, Sabatini R, Abdulrahim M. Fixed-wing MAV attitude stability in atmospheric turbulence, part 1: Suitability of conventional sensors. Prog Aerosp Sci 2014;70:69–82.

[17] Mohamed A, Watkins S, Clothier R, Abdulrahim M, Massey K, Sabatini R. Fixed-wing MAV attitude stability in atmospheric turbulence—part 2: Investigating biologically-inspired sensors. Prog Aerosp Sci 2014;71:1–13.

[18] Batchelor GK, Townsend AA. Decay of vorticity in isotropic turbulence. Proc R Soc Lond A Math Phys Sci 1947;190(1023):534–50.
[19] Comte-Bellot G, Corrsin S. The use of a contraction to improve the isotropy of grid-generated turbulence. J Fluid Mech 1966;25(4):657–82.
[20] Kurian T, Fransson JHM. Grid-generated turbulence revisited. Fluid Dyn Res 2009;41(2):021403.
[21] Gad-El-Hak M, Corrsin S. Measurements of the nearly isotropic turbulence behind a uniform jet grid. J Fluid Mech 1974;62(1):115–43.
[22] Thormann A, Meneveau C. Decay of homogeneous, nearly isotropic turbulence behind active fractal grids. Phys Fluids 2014;26(2):025112.
[23] Tan S, Xu X, Qi Y, Ni R. Scalings and decay of homogeneous, nearly isotropic turbulence behind a jet array. Phys Rev Fluids 2023;8(2):024603.
[24] Wu X. Inflow turbulence generation methods. Annu Rev Fluid Mech 2017;49(1):23–49.
[25] Lund TS, Wu X, Squires KD. Generation of turbulent inflow data for spatially-developing boundary layer simulations. J Comput Phys 1998;140(2):233–58.
[26] Pierce CD. Progress-variable approach for large-eddy simulation of turbulent combustion [Ph.D. thesis], Stanford Univ.; 2001.
[27] García-Villalba M, Li N, Rodi W, Leschziner MA. Large-eddy simulation of separated flow over a three-dimensional axisymmetric hill. J Fluid Mech 2009;627:55–96.
[28] Juneja A, Lathrop DP, Sreenivasan KR, Stolovitzky G. Synthetic turbulence. Phys Rev E 1994;49(6):5179–94.
[29] Béchara W, Bailly C, Lafon P, Candel SM. Stochastic approach to noise modeling for free turbulent flows. AIAA J 1994;32(3):455–63.
[30] Jarrin N, Benhamadouche S, Laurence D, Prosser R. A synthetic-eddy-method for generating inflow conditions for large-eddy simulations. Int J Heat Fluid Flow 2006;27(4):585–93.
[31] Pamiès M, Weiss P-É, Garnier E, Deck S, Sagaut P. Generation of synthetic turbulent inflow data for large eddy simulation of spatially evolving wall-bounded flows. Phys Fluids 2009;21(4).
[32] Roidl B, Meinke M, Schröder W. A reformulated synthetic turbulence generation method for a zonal RANS–LES method and its application to zero-pressure gradient boundary layers. Int J Heat Fluid Flow 2013;44:28–40.
[33] Klein M, Sadiki A, Janicka J. A digital filter based generation of inflow data for spatially developing direct numerical or large eddy simulations. J Comput Phys 2003;186(2):652–65.
[34] Kempf A, Klein M, Janicka J. Efficient generation of initial- and inflow-conditions for transient turbulent flows in arbitrary geometries. Flow Turbul Combust 2005;74(1):67–84.
[35] Xie Z-T, Castro IP. Efficient generation of inflow conditions for large eddy simulation of street-scale flows. Flow Turbul Combust 2008;81(3):449–70.
[36] Schmidt S, Breuer M. Extended synthetic turbulence inflow generator within a hybrid LES–URANS methodology for the prediction of non–equilibrium wall–bounded flows. Flow Turbul Combust 2015;95(4):669–707.
[37] Bercin KM, Xie Z-T, Turnock SR. Exploration of digital-filter and forward-stepwise synthetic turbulence generators and an improvement for their Skewness–Kurtosis. Comput & Fluids 2018;172:443–66.
[38] Kempf A, Wysocki S, Pettit. An efficient M. Parallel low-storage implementation of Klein's turbulence generator for LES and DNS. Comput & Fluids 2012;60:58–60.
[39] Schmidt S, Breuer M. Source term based synthetic turbulence inflow generator for eddy-resolving predictions of an airfoil flow including a laminar separation bubble. Comput & Fluids 2017;146:1–22.
[40] Breuer M. Effect of inflow turbulence on an airfoil flow with laminar separation bubble: An LES study. Flow Turbul Combust 2018;101(2):433–56.
[41] Djenidi L. Lattice-Boltzmann simulation of grid-generated turbulence. J Fluid Mech 2006;552:13–35.
[42] Nagata K, Suzuki H, Sakai Y, Hayase T, Kubo T. Direct numerical simulation of turbulent mixing in grid-generated turbulence. Phys Scr T 2008;132:014054.
[43] Ertunç O, Özyilmaz N, Lienhart H, Durst F, Beronov K. Homogeneity of turbulence generated by static-grid structures. J Fluid Mech 2010;654:473–500.
[44] Suzuki H, Nagata K, Sakai Y, Hayase T, Hasegawa Y, Ushijima T. Direct numerical simulation of fractal-generated turbulence. Fluid Dyn Res 2013;45(6):061409.
[45] Zhou Y, Nagata K, Sakai Y, Suzuki H, Ito Y, Terashima O, et al. Relevance of turbulence behind the single square grid to turbulence generated by regular- and multiscale-grids. Phys Fluids 2014;26(7).
[46] Catalán JM, Moriche M, Flores O, Garcia-Villalba M. On the settling of a spherical particle in slightly perturbed ambient fluid. Acta Mech 2024;235:2479–93.
[47] Taylor G. The spectrum of turbulence. Proc R Soc Lond A Math Phys Sci 1938;164(919):476–90.
[48] Lavoie P, Djenidi L, Antonia RA. Effects of initial conditions in decaying turbulence generated by passive grids. J Fluid Mech 2007;585:395–420.
[49] Djenidi L, Kamruzzaman M, Antonia RA. Power-law exponent in the transition period of decay in grid turbulence. J Fluid Mech 2015;779:544–55.
[50] Uhlmann M. An immersed boundary method with direct forcing for the simulation of particulate flows. J Comput Phys 2005;209(2):448–76.
[51] Roma AM, Peskin CS, Berger MJ. An adaptive version of the immersed boundary method. J Comput Phys 1999;153(2):509–34.
[52] Moriche M. A numerical study on the aerodynamic forces and the wake stability of flapping flight at low Reynolds number [Ph.D. thesis], Universidad Carlos III de Madrid; 2017.
[53] Moriche M, Flores O, García-Villalba M. On the aerodynamic forces on heaving and pitching airfoils at low Reynolds number. J Fluid Mech 2017;828:395–423.
[54] Gonzalo A. Aerodynamic forces and vortex structures of flapping wings in forward flight [Ph.D. thesis], Universidad Carlos III de Madrid; 2018.
[55] Pope SB. Turbulent flows. Cambridge University Press; 2000.
[56] Hunt JC, Wray AA, Moin P. Eddies, streams, and convergence zones in turbulent flows. In: Studying turbulence using numerical simulation databases, 2. Proceedings of the 1988 summer program. 1988.
[57] Mohamed MS, Larue JC. The decay power law in grid-generated turbulence. J Fluid Mech 1990;219:195.
[58] Olivieri S, Viola F, Mazzino A, Rosti ME. Direct numerical simulation of flapping flags in grid-induced turbulence. Phys Fluids 2021;33(8):085116.
[59] Duong D, Tavoularis S. Grid-generated velocity fields at very small Reynolds numbers. Phys Rev Fluids 2024;9(2):024607.
[60] Krogstad P-Å, Davidson P. Is grid turbulence Saffman turbulence? J Fluid Mech 2010;642:373–94.
[61] Hearst RJ, Lavoie P. Decay of turbulence generated by a square-fractal-element grid. J Fluid Mech 2014;741:567–84.